On the asymmetry of cyclones and anticyclones in the cellular regime of rotating Rayleigh-Bénard convection

Hao Fu[1*] and Shiwei Sun[2]
[1] Department of Earth System Science, Stanford University
[2] School of the Atmospheric Sciences, Nanjing University

* Email: haofu@stanford.edu

This is a preprint for EarthArXiv. The manuscript has been submitted to *Physical Review Fluids*. Subsequent versions may have slight modifications. The authors welcome feedbacks from anyone who reads the manuscript.

On the asymmetry of cyclones and anticyclones in the cellular regime of rotating Rayleigh-Bénard convection

Hao Fu*

Department of Earth System Science,

Stanford University, Stanford, 94305 California

Shiwei Sun†

School of Atmospheric Sciences, Nanjing University, Nanjing, China

(Dated: September 12, 2021)

Abstract

Rotating Rayleigh-Bénard convection (RRBC) denotes the free convection between two parallel plates with a fixed temperature difference, placed in a rotating reference frame. It is a prototype model of geophysical and astrophysical convection. Rotation breaks the symmetry on its rotating axis, making the cyclones and anticyclones unequal in size and magnitude. Such an asymmetry has long been observed in experiments and simulations, but has not been explained with any theoretical model. A theory of such vorticity asymmetry is proposed specifically for the cellular regime, where background rotation is important and convection is weak. The property that columnar updraft and downdraft plumes are densely packed is shown to make the vertical vorticity profile at the vortex center approximately linear with height via thermal wind relation. This simplification of morphology enables a linkage between the vorticity strength of a plume which is quantified by vorticity Rossby number $\mathrm{Ro_V}$, and the vorticity magnitude difference between the cyclonic and anticyclonic ends of plumes which is quantified with a nondimensional asymmetry factor δ. The lowest order relationship between δ and $\mathrm{Ro_V}$ is found to be constrained by vertical vorticity equation alone. An approximate analytical solution is found using asymptotic expansion, which shows that the asymmetry is generated mainly by the vertical advection and stretching of vertical vorticity in fluid interior, and is modified by the Ekman layer dynamics.

I. INTRODUCTION

Fluid motion in a rotating background tends to organize into vortices due to the steering effect of Coriolis force. In a counter-clockwise rotating frame which will be used throughout this paper, the fluid area that has positive and negative vertical vorticity ω_z is referred to as cyclones (CC) and anticyclones (AC) respectively. The strength and fractional area of CC and AC are not statistically identical due to the break of symmetry brought by the ambient rotation which is directional. Rotation does not induce asymmetry when it is very strong or very weak [1, 2], as is evident from a symmetry analysis of Navier-Stokes (N-S) equation. The asymmetry can be due to the vertical advection, tilting and stretching of ω_z, or in another view, centrifugal acceleration and the vertical advection of horizontal

* haofu@stanford.edu

† Current affiliation: Nanjing Joint Institute for Atmospheric Sciences, Chinese Academy of Meteorological Sciences, Nanjing, China

momentum [3]. Methods to quantify the asymmetry include investigating the probability distribution function (PDF) of vertical vorticity ω_z and its skewness [4], the statistics of the angle between vorticity vector and the ambient rotation vector [5], and a direct vorticity magnitude comparison of the CC/AC ensemble if the vortex has a well-defined shape [6, 7].

In the single layer shallow water equation which is the simplest paradigm of the large aspect ratio (width over height) stably-stratified rotating flow, ω_z skews towards negative (stronger AC), because an AC area has thicker water depth, which leads to larger Rossby deformation radius that increases the vortex interaction range. This enhances mergers between ACs and therefore makes them less susceptible to the damping by viscosity [4, 8]. When the relative vorticity is smaller compared to the ambient vorticity (small Rossby number), and the scale of motion becomes comparable to or smaller than Rossby deformation radius (weak layer thickness gradient), the motion is quasi-geostrophic and no CC/AC asymmetry exists [9]. The dominance of AC is also observed in free-evolving continuously stratified rotating flow due to the more efficient merger and vertical alignment that prevent substantial vorticity dissipation [10]. For 3D homogeneous rotating non-stratified turbulence, however, a CC is generally more long-lived and therefore stronger than an AC, mainly because an AC tends to be centrifugally unstable when the magnitude of ω_z is larger than the background vorticity, as well as the effect of elliptical instability [5]. Centrifugal instability also exists in shallow water setup, but it is less effective in destabilizing anticyclones, probably because the vertical motion is weak in such a large aspect ratio setup [11].

In this paper, we focus on the asymmetry in 3D unstably-stratified rotating free convection, which has implications for the dynamics of open ocean convection, rotating cumulus cloud in tropical cyclone, Earth dynamo and star interior [12–15]. The strong vertical motion leads to vigorous vertical advection and stretching of vertical vorticity which is quite different from the stably-stratified flow. We study rotating Rayleigh-Bénard convection (RRBC) which is perhaps the simplest paradigm of rotating convection. It is Boussinesq convection between a pair of parallel warm lower plate and cold upper plate in a rotating frame [16]. RRBC is governed by three independent nondimensional parameters [17]:

$$\mathrm{Ra} = \frac{\beta g \Delta T H^3}{\nu \kappa},\ \mathrm{E} = \frac{\nu}{f H^2},\ \mathrm{Pr} = \frac{\nu}{\kappa}, \tag{1}$$

where β is the thermal expansion coefficient, g is the gravitational acceleration, ΔT is the temperature difference between the bottom and top, H is the depth of the fluid, f is Cori-

olis parameter, ν and κ are the kinematic viscosity and diffusivity respectively. Rayleigh number Ra depicts the relative strength of the destabilizing buoyancy to the viscous and diffusive damping. Ekman number E represents the relative strength between viscous diffusion and rotational constraint, and $(2\mathrm{E})^{1/2}$ denotes the ratio of Ekman layer depth to the total depth. Prandtl number Pr is the ratio of kinematic viscosity to thermal diffusivity. Combining the above dimensionless numbers, a convective Rossby number can be defined as $\mathrm{Ro} = \mathrm{E}(\mathrm{Ra}/\mathrm{Pr})^{1/2}$, which is regarded as a measure of the relative strength of thermal forcing to rotational effect [18].

Vorobieff and Ecke [1] showed that in the case of rapidly rotating convection, where Ro$\ll$1, the vertically-aligned columnar vortices dominate the flow. This phenomenon has been observed in many laboratory experiments [7, 19–23] and numerical simulations [18, 24–28]. The regime of RRBC can be further classified with a reduced Rayleigh number $\widetilde{\mathrm{Ra}}= \mathrm{RaE}^{4/3}$. It represents the extent to which the convective system is supercritical to neutral stability [16, 17]. When $\widetilde{\mathrm{Ra}}$ is small (less than 25 as is indicated by Stellmach et al. [17]), the flow is dominated by quasi-steady densely packed columnar vortices which barely interact with each other, called cellular or geostrophic regime. As $\widetilde{\mathrm{Ra}}$ increases (but less than 70) it comes to convective Taylor column regime. The vortices are packed less densely, more significantly shielded, and vortex interaction remains weak. For higher $\widetilde{\mathrm{Ra}}$ (over 70), organized vortices break into unsteady plumes and could organize into barotropic large-scale vortices due to upscale energy cascade [17].

RRBC is elegant because both its geometry and boundary condition are quite symmetric. When the two plates are both no-slip or both free-slip, the only asymmetric factor is rotation. In RRBC, ω_z was found to skew towards positive vorticity generally [1, 6, 18, 29–33]. Some laboratory experiments reported the skew towards anticyclone due to the centrifugal acceleration of the rotating apparatus [6, 7], a factor that will not be considered in this work. Aside from this, the skew towards positive vorticity has been vaguely explained as being forced near the boundary where cyclones are ejected near the departure plate due to angular momentum convergence (or vorticity stretching) associated with the Ekman pumping and buoyant vertical motion, and are diluted in the fluid interior by turbulent mixing before reaching the destination plate [1, 6, 18, 30, 32, 33]. Another factor is inertial instability which restricts the stable anticyclonic vertical vorticity magnitude to be smaller than f, and is especially clear-cut for the cellular regime where vortices are close to circular

[32]. We are not aware of any theoretical model that quantitatively predicts the asymmetry in any regime. The relative contribution of Ekman pumping and the fluid interior factors to the asymmetry remains unknown.

We focus on the cellular regime which is weakly nonlinear, nonturbulent and has small Ro. We avoid inertial instability by considering only the weakly-convective (smaller Ro and $\widetilde{\mathrm{Ra}}$) cases where $\omega_z > -f$ is always met. Portegies et al. [26] showed that a breaking of ω_z symmetry does exist: within an updraft or downdraft in the cellular regime, the CC part has larger vorticity magnitude than the AC part, but this feature has not been explained. There are two candidate analytical vortex models for the cellular regime. One is by Portegies et al. [26] who solved the neutrally-stable mode of a linearized RRBC stability problem in cylindrical coordinate, and the other one is by Grooms et al. [28] who obtained a steady solution of non-hydrostatic quasi-geostrophic equation (NHQG) [25] and considered the nonlinear vertical advection by columnar vortices in shaping the basic state temperature. Both used no-slip vertical boundary condition. They indicated that the main balance of vertical vorticity equation in fluid interior is the stretching of background vorticity and the horizontal diffusion of vertical relative vorticity. The lowest order balance of horizontal vorticity is close to but not the exact thermal wind balance due to the nonhydrostatic effect in such a small-aspect ratio vortex [21, 25]. Neither of the models have considered CC/AC asymmetry. For Portegies *et al.* [26], the asymmetry naturally vanishes in the small-amplitude problem. For Grooms *et al.* [28], NHQG as a finite-amplitude model retains the horizontal advection of ω_z but neglects the vertical advection, stretching and tilting of ω_z. This treatment, which is derived from rigorous multiscale expansion, can capture the basic flow pattern [17]. However, the opportunity for understanding the ω_z asymmetry is missed.

To find the asymmetry, a natural path is using the first order solution (linear instability) to derive the complete next order one. However, the first order solution itself is only semi-analytical, so this path is hard to provide any insight. We notice that the ω_z profile of the vortex center has been found quasi-linear with height [26], but why? If it is robust, can we adopt this linear ω_z profile as an approximation? With this in mind, we establish an analytical model of asymmetry which uses the vertically-averaged CC/AC vortex center ω_z as the asymmetry norm. Three types of boundary conditions are considered to delineate the relative roles of the fluid interior dynamics (vertical advection and stretching of ω_z) and Ekman layer dynamics: both plates no-slip (NN), both free-slip (FF), and a mixed one

(NF). A series of direct numerical simulations (DNS) of RRBC are performed to test the theoretical model.

The paper is organized in the following way. Section II introduces the governing equations and the DNS settings. Section III introduces the theoretical model of vorticity asymmetry and its comparison with DNS. Section IV discusses the physical understanding, and section V concludes the paper.

II. THE GOVERNING EQUATIONS AND DNS SETUP

The dimensional variables are denoted with "*". Let $\widehat{\mathbf{x}}$, $\widehat{\mathbf{y}}$, $\widehat{\mathbf{z}}$ be the unit vectors of Cartesian coordinate, $\mathbf{x}^*$ be the position vector, $\mathbf{u}^* = (u^*, v^*, w^*)$ be the velocity, p^* be the pressure potential, θ'^* be the disturbance temperature that has subtracted a diffusive-equilibrium linear temperature profile, $\omega^* = (\omega_x^*, \omega_y^*, \omega_z^*)$ be the vorticity with $\omega^* = \nabla^* \times \mathbf{u}^*$, where $\nabla^* = \widehat{\mathbf{x}}\partial/\partial x^* + \widehat{\mathbf{y}}\partial/\partial y^* + \widehat{\mathbf{z}}\partial/\partial z^*$ is the gradient operator. Following [26], the variables are nondimensionalized for the DNS. The convective (overturning) time scale is H/W, where the characteristic vertical velocity W uses free-fall scaling $W = \sqrt{g\beta\Delta T H}$. The length scale is domain height H. The temperature scale is ΔT.

$$t^* = tH/W, \quad (x^*, y^*, z^*) = (x, y, z)H, \quad \mathbf{u}^* = \mathbf{u}W, \quad \omega^* = \omega W/H, \quad \theta'^* = \theta'\Delta T, \quad p^* = pW^2. \tag{2}$$

The convection is between a warm plate at $z = -1/2$ and a cold plate at $z = 1/2$, with a doubly-periodic side boundary. The flow obeys the Boussinesq equation:

$$\frac{\partial \mathbf{u}}{\partial t} + (\mathbf{u}\cdot\nabla)\,\mathbf{u} + \mathrm{Ro}^{-1}\widehat{\mathbf{z}} \times \mathbf{u} = -\nabla p + \theta'\widehat{\mathbf{z}} + \left(\frac{\mathrm{Pr}}{\mathrm{Ra}}\right)^{1/2}\nabla^2\mathbf{u}, \tag{3}$$

$$\frac{\partial \theta'}{\partial t} + (\mathbf{u}\cdot\nabla)\,\theta' - w = (\mathrm{PrRa})^{-1/2}\nabla^2\theta', \tag{4}$$

$$\nabla\cdot\mathbf{u} = 0, \tag{5}$$

where $\nabla = \widehat{\mathbf{x}}\partial/\partial x + \widehat{\mathbf{y}}\partial/\partial y + \widehat{\mathbf{z}}\partial/\partial z$ is the nondimensional gradient operator. Note we have convective Rossby number $\mathrm{Ro} \equiv W/(fH) = \mathrm{E}(\mathrm{Ra}/\mathrm{Pr})^{1/2}$. The disturbance temperature boundary condition is Dirichlet:

$$\theta'|_{z=\pm 1/2} = 0. \tag{6}$$

The impermeable velocity boundary condition is:

$$\widehat{\mathbf{z}}\cdot\mathbf{u}|_{z=\pm 1/2} = 0. \tag{7}$$

We study three types of tangential velocity boundary conditions, no-slip-no-slip (NN), free-slip-free-slip (FF) and no-slip-free-slip (NF):

$$\begin{cases} \text{NN}: \quad \widehat{\mathbf{z}} \times \mathbf{u}|_{z=\pm 1/2} = 0, \\ \text{FF}: \quad \widehat{\mathbf{z}} \times \frac{\partial \mathbf{u}}{\partial z}|_{z=\pm 1/2} = 0, \\ \text{NF}: \quad \widehat{\mathbf{z}} \times \mathbf{u}|_{z=-1/2} = 0, \quad \widehat{\mathbf{z}} \times \frac{\partial \mathbf{u}}{\partial z}|_{z=1/2} = 0. \end{cases} \tag{8}$$

The NF case may have implications for penetrative convection in the atmosphere where only the lower surface provides frictional drag, i.e., the tropospheric deep convection penetrating into the stably-stratified stratosphere, or the boundary layer convection penetrating into the capping inversion layer [34]. Approximating the stably-stratified upper layer as a free-slip lid is a usual theoretical practice [35, 36]. However, Moeng and Rotunno [37] argued that a no-slip upper lid is better at reproducing the upper level's positive vertical velocity skewness due to the similar role of a no-slip lid and a stable layer in diminishing momentum.

The DNS is conducted with the Boussinesq solver of Cloud Model 1, version 19.8 (CM1 model) [38]. See Appendix A for the detailed numerical setting. The simulation is run in a $[0, 2.5] \times [0, 2.5] \times [-1/2, 1/2]$ horizontally doubly-periodic domain. We fix $\mathrm{Pr} = 1$ which represents air and is physically simple, but change E and Ra. The reference case uses $\mathrm{Ra} = 2.5 \times 10^6$ and $\mathrm{E} = 10^{-4}$, which is the parameter carefully investigated by Portegies et al. [26]. We perturb Ra and E around this case. Table I shows the specific values of Ra and E for each run, as well as the corresponding Ro and $\widetilde{\mathrm{Ra}}$. Some additional high E tests are arranged for FF type because its convection is generally weaker than other types. All the reduced Rayleigh number $\widetilde{\mathrm{Ra}} = \mathrm{RaE}^{4/3}$ are smaller than 20, so convection is in cellular regime. All the data for analysis is at $t = 110$ (units of overturning timescales) snapshot where convection is in quasi-equilibrium state, though some oscillation still exists.

III. A THEORETICAL MODEL OF ASYMMETRY

A. The simplification of vertical vorticity equation

To make the discussion based on the nondimensional argument more general, we define equivalent Coriolis parameter f_e, depth H_e, viscosity ν_e and diffusivity κ_e:

$$f_e = \mathrm{Ro}^{-1}, \quad H_e = 1, \quad \nu_e = \left(\frac{\mathrm{Pr}}{\mathrm{Ra}}\right)^{1/2}, \quad \kappa_e = (\mathrm{PrRa})^{-1/2}. \tag{9}$$

TABLE I. The Ra, E, Ro, $\widetilde{\mathrm{Ra}}$ and boundary type in the 16 numerical experiments. Pr is fixed at 1. The reference test EXP 4 has $\mathrm{E} = 10^{-4}$ and $\mathrm{Ra} = 2.5 \times 10^6$. The FF (free slip-free slip) tests are run for larger E to guarantee that convection does not decay. EXP 1 - EXP 10 change E and fix Ra. EXP 11 - EXP 16 change Ra and fix E.

Case	$\mathrm{Ra}(\times 2.5 \times 10^6)$	$\mathrm{E}(\times 10^{-4})$	Ro	$\widetilde{\mathrm{Ra}}$	Boundary type
EXP 1	1.00	$0.85^{-1} \approx 1.18$	0.186	14.4	FF
EXP 2	1.00	$0.90^{-1} \approx 1.11$	0.176	13.4	NN/FF/NF
EXP 3	1.00	$0.95^{-1} \approx 1.05$	0.166	12.4	NN/FF/NF
EXP 4	1.00	1.00	0.158	11.6	NN/FF/NF
EXP 5	1.00	$1.05^{-1} \approx 0.95$	0.151	10.9	NN/FF/NF
EXP 6	1.00	$1.10^{-1} \approx 0.91$	0.144	10.2	NN/FF/NF
EXP 7	1.00	$1.15^{-1} \approx 0.87$	0.137	9.6	NN/FF/NF
EXP 8	1.00	$1.20^{-1} \approx 0.83$	0.132	9.1	NN/FF/NF
EXP 9	1.00	$1.25^{-1} = 0.80$	0.126	8.6	NN/NF
EXP 10	1.00	$1.30^{-1} \approx 0.77$	0.122	8.2	NN/NF
EXP 11	$0.9^{-1} \approx 1.11$	1.00	0.167	12.9	NN/FF/NF
EXP 12	$0.95^{-1} \approx 1.05$	1.00	0.162	12.2	NN/FF/NF
EXP 13	$1.05^{-1} \approx 0.95$	1.00	0.154	11.1	NN/FF/NF
EXP 14	$1.10^{-1} \approx 0.91$	1.00	0.151	10.5	NN/FF/NF
EXP 15	$1.15^{-1} \approx 0.87$	1.00	0.147	10.1	NN/FF/NF
EXP 16	$1.20^{-1} \approx 0.83$	1.00	0.144	9.7	NN/FF/NF

They are all nondimensional parameters, but are in a similar form to the original dimensional system.

The flow field is filled with three-dimensional (3D) columnar vortices which are either updraft or downdraft. The vortices are moving slowly and randomly, but they are long-lived and have quasi-steady strength. Warm core updraft (cold core downdraft) vortices are cyclones (anticyclones) at the lower-layer and anticyclones (cyclones) at the upper-layer, as is illustrated in Fig. 1 and Fig. 2 for the reference case (EXP 4). Most like-sign vortices have similar size and strength, but there is an asymmetry inside a columnar vortex: the cyclonic

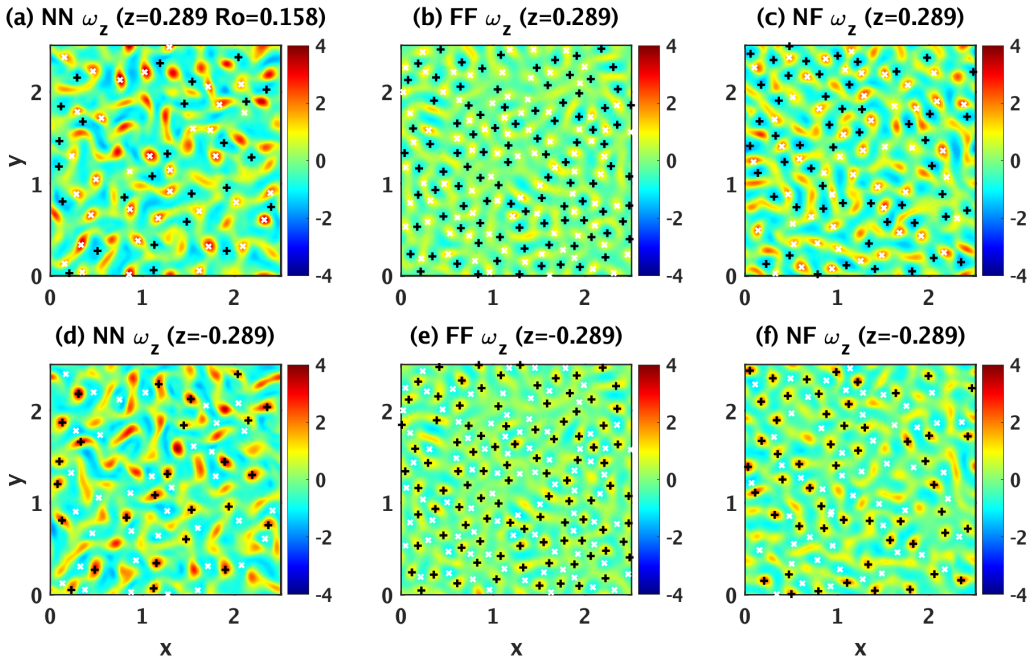

FIG. 1. The contour plotting of the horizontal slice of ω_z for the reference case Ro = 0.158 (EXP 4) at $z/H_e = 0.289$ (upper row) and $z/H_e = -0.289$ (lower row). The left column (a) (d) is NN boundary type, the middle column (b) (e) is FF type, and the right column (c) (f) is NF type. Here the black "+" denotes a detected and successfully paired updraft plume center, and the white "x" denotes a corresponding downdraft plume center.

part is generally stronger and compacter than the anticyclonic part. As the convective amplitude is relatively small, the vortices are approximately erect, axisymmetric and have approximately variable-separation structure in the vertical and radial direction [26]. Thus, understanding the asymmetry can be split into two tasks: understanding the asymmetry of the vortex center and the radial structure respectively. This paper focuses on the former but also takes the latter into account.

The asymmetry at the vortex center was first revealed by Portegies et al. [26] who made an ensemble of vortex center ω_z and w vertical profile to validate their symmetric vortex model. We follow this approach and presented the ensemble average profiles diagnosed from our DNS in Fig. 3 for all the three boundary types. The vortex center detection algorithm used here is introduced in Appendix B. Fig. 3 shows that the ensemble standard deviation of ω_z is relatively small and that of w is larger. Both are smaller for the smaller Ro test which has a weaker convective amplitude in the equilibrium state. Note that the ensemble-

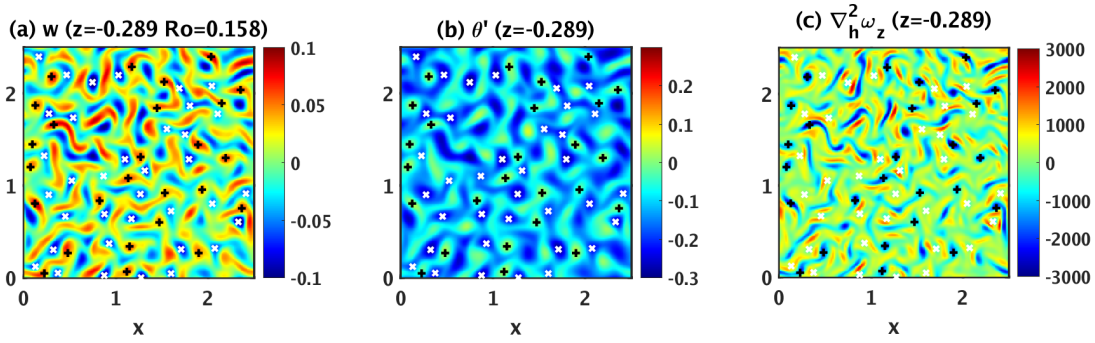

FIG. 2. For the NN type boundary condition of the reference test (EXP 4), (a) the contour plotting of the horizontal slice of vertical velocity w at $z/H_e = -0.289$, (b) disturbance temperature θ', (c) the horizontal Laplace of vertical vorticity $\nabla_h^2\omega_z = \partial^2\omega_z/\partial x^2 + \partial^2\omega_z/\partial y^2$. The rank of sharpness is: $\nabla_h^2\omega_z > \omega_z \sim w > \theta'$, because ∇_h^2 operator has a sharpening effect. The sharpness difference of θ' and ω_z is evident from the thermal wind vorticity equation Eq. (D1) where $\nabla_h^2\theta' \sim f_e\partial\omega_z/\partial z$.

averaged vortex is not a "real vortex" that exactly obeys N-S equation, because the nonlinear advection terms in the governing equation do not commute with the average operator. However, as the budget of ω_z equation (shown in Fig. 4) is approximately balanced, we assume the ensemble-average vortex to obey N-S equation and use it as a reference for theoretical modeling. Fig. 1 and Fig. 2 show that the horizontal position of the vorticity extremums generally coincide with those of w and θ', so "vorticity center" and "updraft/downdraft center" will be regarded as the same object in this paper and is named "vortex center".

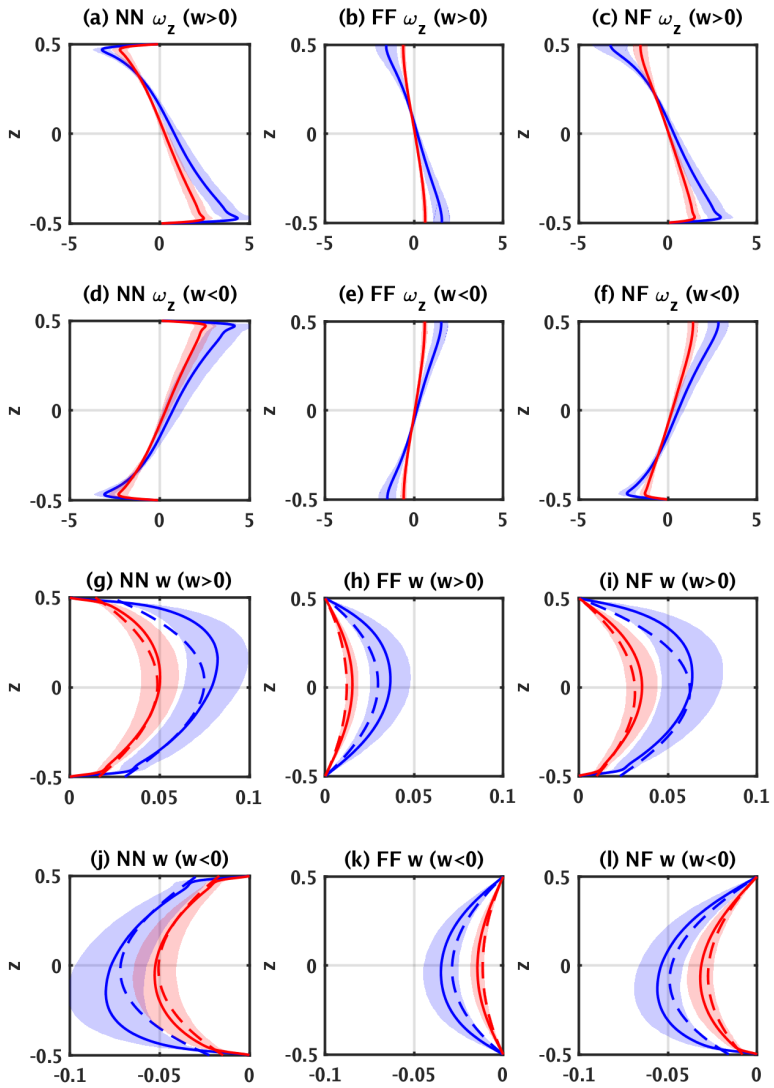

FIG. 3. The vortex center profile of ω_z (the upper two rows) and w (the lower two rows) for the three boundary types NN (left column), FF (middle column) and NF (right column). The first row denotes ω_z for updraft, the second row denotes ω_z for downdraft, the third row denotes w for updraft, and the fourth row denotes w for downdraft. The solid lines denote the ensemble-averaged profiles from our DNS, the shadow denotes the ± 1 standard deviation of the ensemble, and the dashed lines denote those reconstructed from the theory which uses $w = \Delta\omega_z \left(w^{(0)} + \mathrm{Ro_V} w^{(1)}\right)$ and $\omega_z = \Delta\omega_z \left(\delta^{(0)} + \mathrm{Ro_V}\delta^{(1)} - \epsilon_w z\right)$. For all of the subplots, the blue lines and shadow denote the test with a convective Rossby number of $\mathrm{Ro} = 0.158$ (EXP 4) and the red ones denote the $\mathrm{Ro} = 0.132$ (EXP 8) test.

We use the steady state ω_z equation at the vortex center as the main tool:

$$w\frac{\partial \omega_z}{\partial z} = (\omega_z + f_e)\frac{\partial w}{\partial z} + \nu_e \nabla_h^2 \omega_z + \nu_e \frac{\partial^2 \omega_z}{\partial z^2}, \quad \text{where} \quad \nabla_h^2 = \frac{\partial^2}{\partial x^2} + \frac{\partial^2}{\partial y^2}. \tag{10}$$

As the vortex center line is approximately vertical, there is no horizontal advection and tilting. Eq. (10) is a powerful constraint of ω_z and w, though not enough to determine the full dynamics, especially convective strength. The vortices' small aspect ratio makes horizontal vorticity diffusion much larger than vertical diffusion in fluid interior, so $\nu_e \partial^2 \omega_z / \partial z^2$ can be neglected there [25]. For an updraft, the positive ω_z is produced by the stretching of $(\omega_z + f_e)$ at the lower layer. As the parcel moves up, ω_z is dissipated by horizontal diffusion to be close to 0 at the middle plane, and it further decreases to negative value at the upper-layer due to the squeezing of $(\omega_z + f_e)$. For the small Ro case where $\omega_z \ll f_e$, the vertical advection and stretching of ω_z are small terms, so the primary fluid interior balance is:

$$f_e \frac{\partial w}{\partial z} \sim -\nu_e \nabla_h^2 \omega_z. \tag{11}$$

The remaining balance between ambient vorticity stretching and horizontal diffusion tends to render a vertically antisymmetric ω_z and a symmetric w [39]. Should the CC/AC asymmetry be due to the finite Ro effect in Eq. (10)? With this in mind, we further simplify the ω_z equation and its boundary condition.

For no-slip boundary, there is an Ekman layer that links the nearly geostrophic interior with large ω_z to the zero ω_z at the boundary. Vertical diffusion of ω_z approximately balances the stretching of background vorticity, yielding a non-growing boundary layer depth of $(2\mathrm{E})^{1/2} H_e$:

$$f_e \frac{\partial w}{\partial z} \sim -\nu_e \frac{\partial^2 \omega_z}{\partial z^2}. \tag{12}$$

For the $\mathrm{Ro} \ll 1$ case, both the vertical advection and stretching of ω_z in the Ekman layer are small terms. As Ekman layer is very thin ($\mathrm{E}^{1/2} \ll 1$), Eq. (12) leads to a parameterization using Ekman pumping relation that links the w and ω_z at the Ekman layer top [17, 39, 40], as if the boundary is penetrative. All of them use the linear Ekman layer theory for $\mathrm{Ro} \ll 1$ case, which renders symmetric CC/AC and does capture the lowest order dynamics. However, the small vertical advection and stretching of ω_z also contribute to the asymmetry in Ekman layer, enhancing suction by AC and weakening pumping by CC. Ishida and Iwayama [41] used asymptotic expansion to show that the stretching of ω_z strengthens the existing ω_z and the vertical advection of ω_z weakens it for both CC and AC. As the

stretching dominates the advection, their net ω_z production shares the burden of the f_e stretching for CC but add some for AC. As a result, the vertical integral of $|f_e \partial w/\partial z|$ within the Ekman layer and therefore the Ekman layer top $|w|$ is smaller for CC than AC. The asymmetry could also be related to the centrifugal acceleration that decelerates (accelerates) the converging (diverging) fluid [42]. We adopt the first order truncation of the asymptotic Ekman pumping formula for a circular vortex derived by Hart [43]:

$$
\begin{aligned}
w|_{z=-H_e/2} &= \epsilon_b \left(\frac{\mathrm{E}}{2}\right)^{\frac{1}{2}} H_e \omega_z \left(1 - \gamma \frac{\omega_z}{f_e}\right)|_{z=-H_e/2}, \\
w|_{z=H_e/2} &= -\epsilon_t \left(\frac{\mathrm{E}}{2}\right)^{1/2} H_e \omega_z \left(1 - \gamma \frac{\omega_z}{f_e}\right)|_{z=H_e/2}.
\end{aligned} \tag{13}
$$

Here $z = \pm H_e/2$ denotes the boundary layer top rather than the solid wall. The $\gamma = 1/5$ is a constant; ϵ_b and ϵ_t are used to denote no-slip and free-slip boundary condition at the lower and upper plate respectively:

$$
\epsilon_b,\, \epsilon_t = \begin{cases} 1, & \mathrm{no-slip} \\ 0, & \mathrm{free-slip} \end{cases}. \tag{14}
$$

The derivation and validation of Eq. (13) is shown in Appendix C.

Fig. 3 shows that the vortex center ω_z approximately changes linearly with z in fluid interior for all the three boundary types. Such a quasi-linear profile appears in the DNS of Portegies et al. [26] for NN boundary type and has been reproduced by the neutral mode of their linear stability analysis. For FF type, the linear stability analysis [16] shows $\omega_z \sim \pm\sin(\pi z)$, agreeing with our DNS result in Fig. 3. It is also not far from a linear profile. The NF type profile looks like a mixture of the NN and FF ones. In Appendix D, the quasi-linear shape is explained with the advective-diffusive equilibrium of temperature field and thermal wind relation, as is also illustrated in the schematic diagram in Fig. 5. This feature inspires us to fit the vortex center ω_z (outside of the boundary layer) using a linear function of z with two unknown parameters $\overline{\omega_z}$ and $\Delta\omega_z$:

$$
\omega_z = \overline{\omega_z} - \epsilon_w \Delta\omega_z \frac{z}{H_e},\ \epsilon_w = \begin{cases} 1 & w > 0 \\ -1 & w < 0 \end{cases}. \tag{15}
$$

Here ϵ_w is used to signify updraft or downdraft, $\overline{\omega_z}$ is the intercept which denotes the vertical average of ω_z at fluid interior, $\Delta\omega_z$ represents the slope which denotes the vertical vorticity

magnitude. An asymmetry factor δ which is $\overline{\omega_z}$ normalized by $\Delta\omega_z$ is defined to quantify the asymmetry of the vortex center ω_z profile:

$$\delta \equiv \frac{\overline{\omega_z}}{\Delta\omega_z}. \tag{16}$$

The $\Delta\omega_z$ contains information of the convective strength that cannot be solely constrained by the ω_z equation. Geometrically, δ is the shift of $\omega_z = 0$ height from the middle plane $z = 0$. It is also linked to the ratio of AC to CC vorticity magnitude at the Ekman layer top where their contrast is the largest: $|\delta - 1/2|/|\delta + 1/2| \approx 1 - 4\delta$. Our goal is to solve δ. In our work, $\Delta\omega_z$ is directly diagnosed from DNS. To theoretically estimate $\Delta\omega_z$, one can try the finite-amplitude vortex model which tells the amplitude and wavenumber at the same time [28]. See section III C for further discussion.

Now we consider the radial ω_z structure in a vortex which determines the vortex center $\nabla_h^2\omega_z$. This involves the CC/AC asymmetry in the radial structure. Fig. 2(c) shows the $\nabla_h^2\omega_z$ at $z = -0.289H_e$ which is within the lower layer. It's not surprising that the $\nabla_h^2\omega_z$ for updraft vortices is negative, indicating that horizontal viscosity reduces ω_z magnitude. However, the $\nabla_h^2\omega_z$ of downdraft vortices is close to 0. The highest $\nabla_h^2\omega_z$ is not at the updraft centers, but surrounding them in a petal shape. The budget of ω_z equation at the vortex center in Fig. 4 shows that the updraft core's $\nabla_h^2\omega_z$ of the reference test is also quasi-linear with height, but it is mostly negative. To explain this, we note that for doubly periodic domain the horizontally integrated ω_z at any height should be 0: $\iint \omega_z dxdy = 0$. This makes cyclones which are larger in magnitude have smaller fractional area, and vice versa for anticyclones, as was first noticed by Julien et al. [18] and is illustrated here in the left panel of Fig. 5 as a schematic diagram. We speculate that the contraction (expansion) of vortex area at a CC (AC) might be partly driven by the pushing of the horizontally convergent (divergent) flow. The petal shape $\nabla_h^2\omega_z$ patch could be the vortex shield of the strong cyclones which has been predicted in the vortex models of Portegies et al. [26] and Grooms et al. [28], and has been experimentally verified by Shi et al. [7]. It is not a closed donut in Fig. 2(c) due to the straining of the neighboring vortices that breaks the axisymmetry. As anticyclones are weak, the cyclones' shield ω_z (<0) can outweigh and surround the anticyclones' core vorticity ω_z (<0), making $\nabla_h^2\omega_z$ remain negative. We present an approximation of the $\nabla_h^2\omega_z$ profile by grasping its upper and lower ends. There, the vortex center vorticity still outweighs the neighbor's shield vorticity, with $\nabla_h^2\omega_z$ and ω_z

having opposite sign. At both ends, we let the length scale for ∇_h^2 at a CC (AC) center be L_+ (L_-). Using Eq. (15), $\nabla_h^2\omega_z$ is estimated as:

$$\nabla_h^2\omega_z \approx \frac{1}{2}\left(\nabla_h^2\omega_z|_{\mathrm{CC}} + \nabla_h^2\omega_z|_{\mathrm{AC}}\right) - \epsilon_w\left(\nabla_h^2\omega_z|_{\mathrm{CC}} - \nabla_h^2\omega_z|_{\mathrm{AC}}\right)\frac{z}{H_e}, \tag{17}$$

where $\nabla_h^2\omega_z|_{\mathrm{CC}}$ ($\nabla_h^2\omega_z|_{\mathrm{AC}}$) is $\nabla_h^2\omega_z$ at the cyclonic (anticyclonic) end:

$$\nabla_h^2\omega_z|_{\mathrm{CC}} \approx -\alpha\frac{\overline{\omega_z} + \frac{1}{2}\Delta\omega_z}{L_+^2}, \quad \nabla_h^2\omega_z|_{\mathrm{AC}} \approx -\alpha\frac{\overline{\omega_z} - \frac{1}{2}\Delta\omega_z}{L_-^2}. \tag{18}$$

Here α is a nondimensional shape factor. Portegies et al. [26] and Shi et al. [7] have shown that the horizontal structure of ω_z in the cellular regime approximately obeys zeroth order Bessel function $J_0(kr)$ where k is the eigenvalue and r is the radial distance from vortex center. The corresponding Bessel equation yields $\nabla_h^2\omega_z = -k^2\omega_z$ at the vortex center. Let the first zero point ($kr \approx 2.4$) of ω_z be half of L_d, we get $kL_d/2 \approx 2.4$, and therefore $\alpha \approx 23$ which is used in this model. L_+ and L_- depends on CC/AC fractional area which is linked to CC/AC vorticity magnitude via $\iint \omega_z dxdy = 0$:

$$\frac{L_+^2}{L_-^2} = \frac{\left|\overline{\omega_z} - \frac{1}{2}\Delta\omega_z\right|}{\left|\overline{\omega_z} + \frac{1}{2}\Delta\omega_z\right|} = \frac{\frac{1}{2} - \delta}{\frac{1}{2} + \delta}. \tag{19}$$

Suppose the number density of AC and CC are identical, the vortex distance scale L_d can be interpreted as the length scale corresponding to the mean fractional area (proportional to the square of length scale) of AC and CC:

$$L_d^2 = \frac{1}{2}\left(L_+^2 + L_-^2\right). \tag{20}$$

Substituting Eqs. (18), (19), and (20) into Eq. (17), and using $\delta \ll 1$, we get an approximate expression of $\nabla_h^2\omega_z$ which has $O(\delta^2)$ error:

$$\nabla_h^2\omega_z \approx -\alpha\frac{\Delta\omega_z}{L_d^2}(2\delta - \epsilon_w\frac{z}{H_e}). \tag{21}$$

Thus, $-\nabla_h^2\omega_z \sim (2\delta - \epsilon_w z/H_e)$ skews more towards positive than $\omega_z \sim (\delta - \epsilon_w z/H_e)$, due to the additional effect of the changing radial structure. This indicates that the $\nabla_h^2\omega_z = 0$ height is farther from the mid-plane than that of $\omega_z = 0$, in agreement with the DNS result which is illustrated in the budget plotting in Fig. 4 for updrafts. Note that our argument in deriving Eq. (21) requires the symmetry between an updraft and downdraft, which is not strictly met for the NF type. The error is not significant in Fig. 4(c) and (f), but it is indeed an unresolved flaw.

Substituting Eqs. (15) and (21) into Eq. (10), the vertical vorticity equation is simplified to a first order ODE about vortex center w with one unknown parameter $\overline{\omega_z}$ (or δ) and two given parameters $\Delta\omega_z$ and L_d which are diagnosed from DNS. This, together with the two boundary conditions which is obtained by substituting Eq. (15) into Eq. (13), render a deterministic problem:

$$
\begin{aligned}
w\left(-\epsilon_w\frac{\Delta\omega_z}{H_e}\right) &= \left(\overline{\omega_z}-\epsilon_w\Delta\omega_z\frac{z}{H_e}+f_e\right)\frac{dw}{dz}-\alpha\frac{\nu_e\Delta\omega_z}{L_d^2}\left(2\delta-\epsilon_w\frac{z}{H_e}\right), z\in\left(-\frac{H_e}{2},\frac{H_e}{2}\right),\\
w|_{z=-\frac{1}{2}H_e} &= \epsilon_b\left(\frac{\mathrm{E}}{2}\right)^{\frac{1}{2}}H_e\left(\overline{\omega_z}+\frac{\epsilon_w\Delta\omega_z}{2}\right)\left[1-\left(\overline{\omega_z}+\frac{\epsilon_w\Delta\omega_z}{2}\right)\frac{\gamma}{f_e}\right],\\
w|_{z=\frac{1}{2}H_e} &= -\epsilon_t\left(\frac{\mathrm{E}}{2}\right)^{\frac{1}{2}}H_e\left(\overline{\omega_z}-\frac{\epsilon_w\Delta\omega_z}{2}\right)\left[1-\left(\overline{\omega_z}-\frac{\epsilon_w\Delta\omega_z}{2}\right)\frac{\gamma}{f_e}\right].
\end{aligned}
\tag{22}
$$

One might speculate: how can a first order ODE satisfy two boundary conditions? In fact, such an overdetermined problem can be avoided by setting δ a proper value, which renders a nonlinear eigenvalue problem. In other words, the δ which stands for CC/AC asymmetry can be solved from the solvability condition, as is derived in section III B below. The asymmetry is produced by both the ODE which depicts the fluid interior dynamics and the Ekman layer boundary conditions.

B. Solving the asymmetry factor δ

Because the vortex magnitude which is measured by $\Delta\omega_z$ is an input parameter for the asymmetry problem, w and ω_z are rescaled with $\Delta\omega_z$, yielding the new variables w^+ and ω_z^+:

$$
w^+ = w/\Delta\omega_z, \quad \omega_z^+ = \omega_z/\Delta\omega_z. \tag{23}
$$

They will be used in the theoretical derivation in this section. Eq. (22) becomes:

$$
\begin{aligned}
-\mathrm{Ro_V}\epsilon_w w^+ &= \left[\mathrm{Ro_V}\left(\delta-\epsilon_w z\right)+1\right]\frac{dw^+}{dz}-\frac{\alpha\mathrm{E}}{\Gamma^2}(2\delta-\epsilon_w z),\ z\in\left(-\frac{1}{2},\frac{1}{2}\right),\\
w^+|_{z=-1/2} &= \epsilon_b\left(\frac{\mathrm{E}}{2}\right)^{\frac{1}{2}}\left(\delta+\frac{\epsilon_w}{2}\right)\left[1-\gamma\mathrm{Ro_V}\left(\delta+\frac{\epsilon_w}{2}\right)\right],\\
w^+|_{z=1/2} &= -\epsilon_t\left(\frac{\mathrm{E}}{2}\right)^{1/2}\left(\delta-\frac{\epsilon_w}{2}\right)\left[1-\gamma\mathrm{Ro_V}\left(\delta-\frac{\epsilon_w}{2}\right)\right].
\end{aligned}
\tag{24}
$$

Here $\mathrm{Ro_V}$ is vorticity Rossby number which denotes vorticity magnitude, and Γ is the vortex aspect ratio:

$$
\mathrm{Ro_V}\equiv\frac{\Delta\omega_z}{f_e}, \quad \Gamma\equiv\frac{L_d}{H_e}. \tag{25}
$$

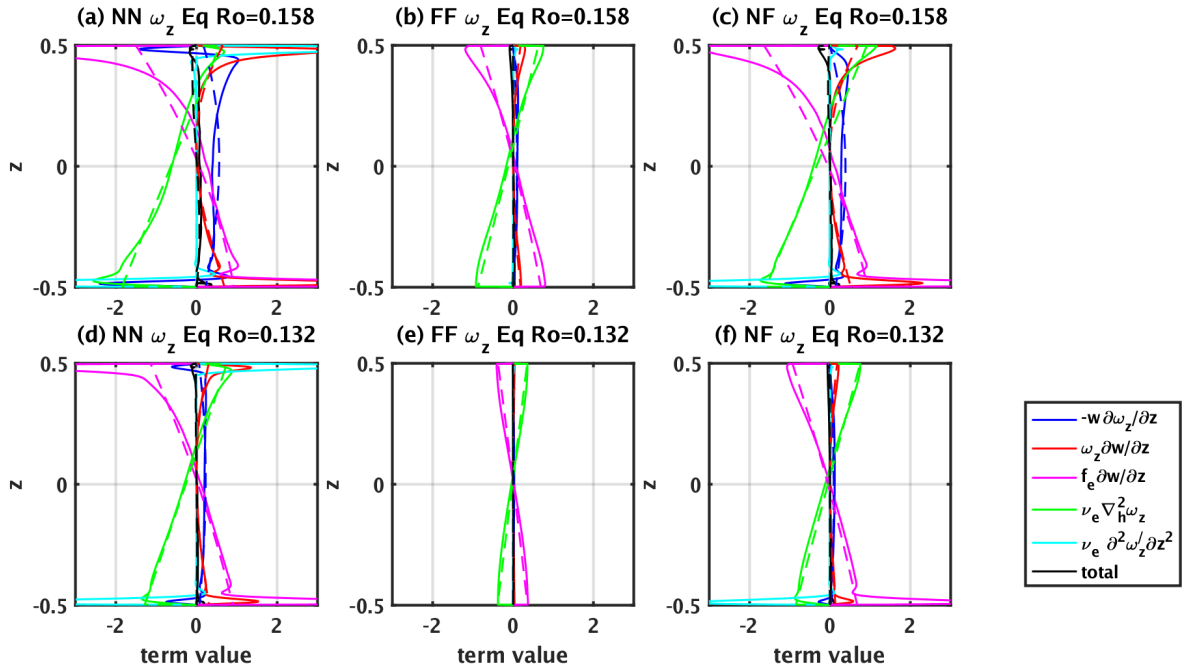

FIG. 4. The budget of ω_z equation along the center of updraft vortices, using nondimensional variables. The solid lines denote the ensemble-averaged profiles from DNS, and the dashed lines denote those reconstructed from the theory which uses $w = \Delta\omega_z \left(w^{(0)} + \mathrm{Ro_V} w^{(1)}\right)$ and $\omega_z = \Delta\omega_z \left(\delta^{(0)} + \mathrm{Ro_V}\delta^{(1)} - \epsilon_w z\right)$. The left column is for NN boundary type, the middle column is for FF type, and the right column is for NF type. The upper row is for Ro = 0.158 (EXP 4), and the lower row is for Ro = 0.132 (EXP 8). The blue line denotes $-w\partial\omega_z/\partial z$, the red line denotes $\omega_z\partial w/\partial z$, the magenta line denotes $f_e\partial w/\partial z$, the green line denotes $\nu_e\nabla_h^2\omega_z$, the cyan line denotes $\nu_e\partial^2\omega_z/\partial z^2$, and the black line denotes the sum of all terms. That the total sum of the diagnosed terms is nearly zero validates the vortex detection method and the quasi-steady assumption. The total sum of the theoretically-calculated terms is not exactly 0, due to the error introduced by asymptotic expansion.

Both numbers are input parameters of the theory. Both the Ekman layer boundary condition and the horizontal diffusion are associated with the viscous coefficient (represented by E), but they have different power dependence on E (order 1/2 and 1). Horizontal diffusion is further modulated by Γ: thinner vortex suffers from stronger diffusion.

Equation (24) renders a nonlinear eigenvalue problem of δ. As $\mathrm{Ro_V} \lesssim 1$ for most of

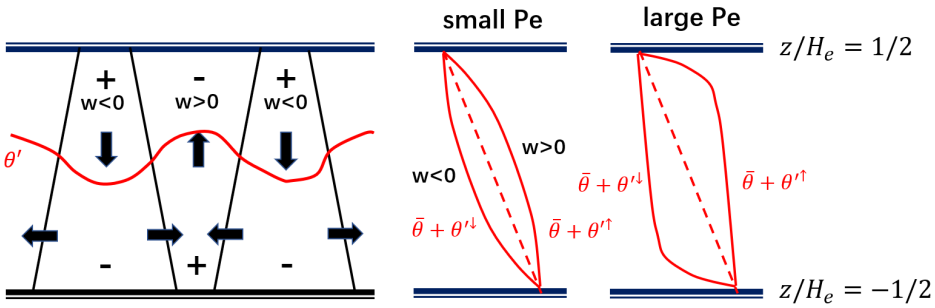

FIG. 5. The left panel is a schematic diagram of the densely packed updraft and downdraft vortices. Updraft (downdraft) vortices are cyclonic (anticyclonic) at the lower- (upper-) level. The fractional area of the cyclonic (anticyclonic) end is small (large) because horizontally averaged ω_z at any height should be 0. The solid red line denotes the temperature contour surface which is pushed upward (downward) by an updraft (downdraft). The middle and right panels are explained in Appendix D. In the middle panel, the two solid red lines denote the temperature at an updraft and downdraft core ($\theta'^{\uparrow} + \overline{\theta}$ and $\theta'^{\downarrow} + \overline{\theta}$) for a small Pe case where diffusion is dominant. Here $\overline{\theta} = -z$ is the basic state temperature profile which is in diffusive equilibrium. The right panel denotes those for a large Pe case where vertical advection dominates. The red dashed line denotes the diffusive-equilibrium temperature profile.

our tests (corresponding to $\widetilde{\mathrm{Ra}} \lesssim 15$ as is shown in Table I), we seek for an approximate analytical solution using asymptotic expansion of $\mathrm{Ro_V}$ to study how δ depends on $\mathrm{Ro_V}$, Γ and E, under three types of boundary condition: NN, FF and NF. The numerical solution of the full equation is quite opaque to physical understanding but can be used to validate the asymptotic solution, as is introduced in Appendix E. Let δ and w be approximated as a power series of $\mathrm{Ro_V}$:

$$\delta = \delta^{(0)} + \mathrm{Ro_V}\delta^{(1)} + \mathrm{Ro_V^2}\delta^{(2)} \ldots, \quad w^{+} = w^{(0)} + \mathrm{Ro_V} w^{(1)} + \mathrm{Ro_V^2} w^{(2)} \ldots. \tag{26}$$

Here the superscripts $^{(0)}$, $^{(1)}$ and $^{(2)}$ denote the terms with different $\mathrm{Ro_V}$ orders. Substituting Eq. (26) into Eq. (24), we get the zeroth order ODE and boundary condition:

$$0 = \frac{dw^{(0)}}{dz} + \frac{\alpha \mathrm{E}}{\Gamma^2}\left(\epsilon_w z - 2\delta^{(0)}\right),$$
$$w^{(0)}\,|_{z=-\frac{1}{2}} = \epsilon_b \left(\frac{\mathrm{E}}{2}\right)^{\frac{1}{2}} \left(\frac{\epsilon_w}{2} + \delta^{(0)}\right), \quad w^{(0)}\,|_{z=\frac{1}{2}} = \epsilon_t \left(\frac{\mathrm{E}}{2}\right)^{\frac{1}{2}} \left(\frac{\epsilon_w}{2} - \delta^{(0)}\right). \tag{27}$$

It describes the balance between background vorticity stretching and the horizontal diffusion of vorticity. $\delta^{(0)}$ is solved by enforcing the solvability condition:

$$\delta^{(0)} = \frac{\epsilon_w(\epsilon_t - \epsilon_b)}{4\sqrt{2}\alpha\Gamma^{-2}\mathrm{E}^{1/2} + 2(\epsilon_t + \epsilon_b)} = \frac{\epsilon_w(\epsilon_t - \epsilon_b)}{4\sqrt{2}\alpha\Gamma^{-2}\mathrm{E}^{1/2} + 2}. \tag{28}$$

Equation (28) has used the fact that $\delta^{(0)}$ is only nonzero when the two boundary conditions are of different types, e.g. NF type. There is $\delta^{(0)} \sim 0.03$ for the NF type run of EXP 4. The sign of nonzero $\delta^{(0)}$ is opposite for an updraft and downdraft. For EXP 4, we have $4\sqrt{2}\alpha\Gamma^{-2}\mathrm{E}^{1/2} \approx 33$. Ignoring the "2" in the denominator is equivalent to ignoring the $\delta^{(0)}$ terms in the boundary conditions. Thus, the main role of $\delta^{(0)}$ is regulating the horizontal diffusion term in the fluid interior to absorb the asymmetry produced by the stretching/squeezing difference of background vorticity (f_e), which originates from the Ekman pumping/suction difference. Substituting Eq. (28) into Eq. (27), $w^{(0)}$ is solved:

$$w^{(0)} = \frac{\alpha\mathrm{E}}{\Gamma^2}\left(-\frac{\epsilon_w}{2}z^2 + 2\delta^{(0)}z + \delta^{(0)} + \frac{\epsilon_w}{8}\right) + \epsilon_b\left(\frac{\mathrm{E}}{2}\right)^{\frac{1}{2}}\left(\frac{\epsilon_w}{2} + \delta^{(0)}\right). \tag{29}$$

The $\alpha\mathrm{E}/\Gamma^2$ essentially denotes the relative strength of horizontal diffusion to background vorticity stretching. The last term denotes the extra vertical velocity provided by Ekman pumping. For NN or FF boundary condition where $\delta^{(0)} = 0$, $w^{(0)}$ is a symmetric parabolic line which has the largest magnitude at the middle plane $z = 0$.

The first order equation and boundary conditions are

$$\begin{aligned}
-\epsilon_w w^{(0)} &= \left(\delta^{(0)} - \epsilon_w z\right)\frac{dw^{(0)}}{dz} + \frac{dw^{(1)}}{dz} - \frac{2\alpha\mathrm{E}}{\Gamma^2}\delta^{(1)}, \\
w^{(1)}|_{z=-\frac{1}{2}} &= \epsilon_b\left(\frac{\mathrm{E}}{2}\right)^{1/2}\left[\delta^{(1)} - \gamma\left(\delta^{(0)} + \frac{\epsilon_w}{2}\right)^2\right], \\
w^{(1)}|_{z=\frac{1}{2}} &= -\epsilon_t\left(\frac{\mathrm{E}}{2}\right)^{1/2}\left[\delta^{(1)} - \gamma\left(\delta^{(0)} - \frac{\epsilon_w}{2}\right)^2\right].
\end{aligned} \tag{30}$$

It describes how the vertical advection (the left-hand-side) and stretching of ω_z (the first term on the right-hand-side, RHS) are balanced by the asymmetry in ω_z and w through the stretching of f_e (the second term on the RHS), horizontal diffusion (the third term on the RHS) and the anomalous Ekman pumping/suction. The solvability condition leads to $\delta^{(1)}$ which is generally positive:

$$\delta^{(1)} = \frac{\left[\frac{1}{6} + 2\left(\delta^{(0)}\right)^2 + \delta^{(0)}\epsilon_w\right]\frac{\alpha\mathrm{E}}{\Gamma^2} + \frac{\epsilon_b}{2}\left(\frac{\mathrm{E}}{2}\right)^{1/2} + \gamma\left[\epsilon_b\left(\delta^{(0)} + \frac{\epsilon_w}{2}\right)^2 + \epsilon_t\left(\delta^{(0)} - \frac{\epsilon_w}{2}\right)^2\right]\left(\frac{\mathrm{E}}{2}\right)^{1/2}}{2\frac{\alpha\mathrm{E}}{\Gamma^2} + (\epsilon_b + \epsilon_t)\left(\frac{\mathrm{E}}{2}\right)^{1/2}} \tag{31}$$

The last term in the numerator is the contribution from the nonlinear effects in Ekman layer which makes pumping less efficient in CC than suction in AC. The corresponding $w^{(1)}$ is:

$$w^{(1)}= a\frac{z^3+1/8}{3}+b\frac{z^2-1/4}{2}+c\left(z+\frac{1}{2}\right)+\epsilon_b\left(\frac{\mathrm{E}}{2}\right)^{1/2}\left[\delta^{(1)}-\gamma\left(\delta^{(0)}+\frac{\epsilon_w}{2}\right)^2\right], \quad (32)$$

where the coefficients a, b and c are:

$$\begin{aligned} a&= -\frac{\alpha\mathrm{E}}{2\Gamma^2}, \quad b=\epsilon_w\frac{\alpha\mathrm{E}}{\Gamma^2}\delta^{(0)}, \\ c&= -\frac{\alpha\mathrm{E}}{\Gamma^2}\left\{\frac{1}{8}+\epsilon_w\delta^{(0)}-2\left[\delta^{(1)}-\left(\delta^{(0)}\right)^2\right]\right\}-\epsilon_b\left(\frac{\mathrm{E}}{2}\right)^{1/2}\left(\frac{1}{2}+\epsilon_w\delta^{(0)}\right). \end{aligned} \quad (33)$$

Fig. 6 shows the $w^{(0)}$ and $w^{(1)}$ for Ro = 0.158 case (EXP 4) of the three boundary types. $w^{(1)}$ is an odd function for NN and FF type, which is obvious from a symmetry analysis of Eq. (30). The $w^{(1)}$ tends to shift the extremum of w towards the anticyclonic side, agreeing with the DNS in Fig. 3. However, Fig. 3 also shows that the theory underestimates the magnitude of w for EXP 4 (large Ro test), as well as the asymmetric feature of w as a whole.

As will be shown in the validation against the numerical nonlinear solution in Fig. 8, the first order asymptotic solution renders sufficient accuracy, even for $\mathrm{Ro_V} \gtrsim 1$ cases. We conclude that the difference in boundary condition leads to zeroth order vorticity asymmetry, and a finite $\mathrm{Ro_V}$ leads to first order asymmetry.

C. Comparison of the theory with DNS

In this section we compare the theoretical result $\delta \approx \delta^{(0)} + \mathrm{Ro_V}\delta^{(1)}$ which uses Eqs. (28) and (31) with DNS for NN (no-slip-no-slip), FF (free-slip-free-slip) and NF (no-slip-free-slip) boundary types.

Here we introduce the method of diagnosing $\mathrm{Ro_V} = \Delta\omega_z/f_e$, $\delta = \overline{\omega_z}/\Delta\omega_z$ and $\Gamma{=}L_d/H_e$ from DNS. The $\Delta\omega_z$ and $\overline{\omega_z}$ are diagnosed from the ensemble-averaged vortex center ω_z profile. Their values, as well as $\mathrm{Ro_V}$ and δ are diagnosed separately for updrafts and downdrafts. The $\Delta\omega_z$ is set as the difference between the maximum and minimum ω_z on the profile. The $\overline{\omega_z}$ is set as the numerical vertical average of the ω_z profile. For convenience, it includes the Ekman layer which has tiny contribution to the integral due to its thin depth. Fig. 7(a) shows that there is an approximately monotonic relationship between $\mathrm{Ro_V}$ and $\widetilde{\mathrm{Ra}}$ diagnosed from our data, with NN type having the largest $\mathrm{Ro_V}$, FF type having the smallest

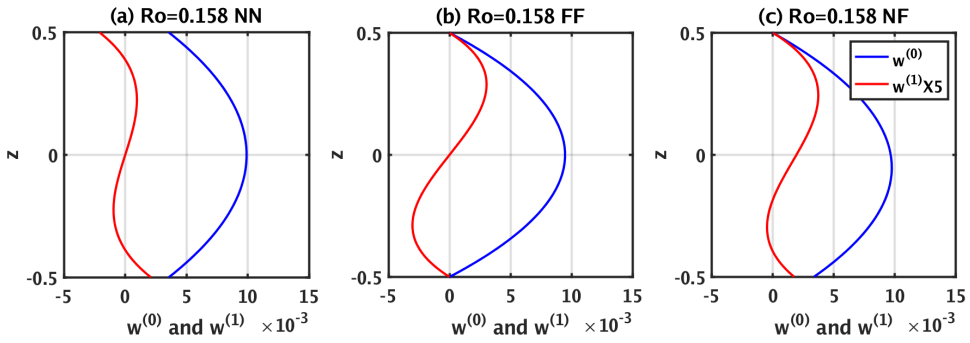

FIG. 6. The $w^{(0)}$ (blue line) and $w^{(1)}$ (red line, multiplied by 5) of the Ro = 0.158 case (EXP 4), for (a) the NN type boundary condition, (b) FF type and (c) the NF type.

and NF type lying between them. To diagnose L_d and therefore Γ, we follow Sakai (1997) to count the vortex number, as is shown in Appendix B. Fig. 7(b) and (c) show that Γ increases mildly with E and Ra. The dependence on E roughly agrees with the FF type neutral mode result $\Gamma \sim \mathrm{E}^{1/3}$ [16]. Physically, a stronger background rotation leads to a stronger tilting of f_e to the tangential direction, which requires a larger baroclinic torque to maintain thermal wind balance. This leads to a smaller vortex size. The dependence on Ra is likely due the nonlinear upscale growth (e.g. vortex merger), where the horizontal scale is larger for a larger convective amplitude. The Γ for NN type is a bit larger than the FF and NF types, probably due to the difference in boundary condition and the convective amplitude.

Except for the $\Gamma \sim \mathrm{E}^{1/3}$ scaling, we will not invoke other theoretical determination of Γ and $\mathrm{Ro_V}$ in this paper. Though Sakai [21] provided a scaling theory of vortex size, it is suitable for more vigorous convection and requires a well-developed thermal boundary layer. The finite-amplitude model of Grooms et al. [28] is also a candidate for determining Γ and

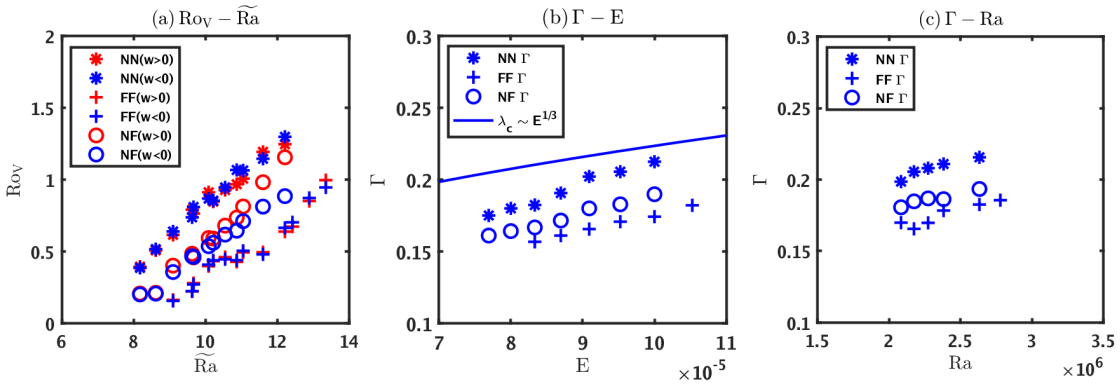

FIG. 7. (a) The dependence of $\mathrm{Ro_V}$ on $\widetilde{\mathrm{Ra}}$ for all the data. The "*" denotes NN boundary type, the "+" denotes FF type, and the "o" denotes NF type. The red marks denote ascending (warm) vortices, and the blue marks denotes descending (cold) vortices. (b) The mean vortex aspect ratio Γ of updraft and downdraft vortices for changing E (EXP 1-10) tests. The blue "*" denotes the Γ diagnosed from DNS for NN type; the blue "+" denotes FF type; the "o" denotes NF type. The solid blue line denotes the $\mathrm{E}^{1/3}$ law which is the most unstable wavelength predicted with the linear stability analysis of FF type: $\lambda_c = 2\pi/k_c = 2^{7/6}\pi^{2/3}\mathrm{E}^{1/3}$ [16]. For a checkerboard vortex pattern, Γ should be compared to $\lambda_c/2$. (c) The same as (b), but for Γ of the changing Ra tests (EXP 11-16). The λ_c is not plotted.

$\mathrm{Ro_V}$, but it does not yield an explicit expression, therefore we leave the coupling of their model to our vorticity asymmetry theory for future work.

Fig. 8 shows the relationship between δ and $\mathrm{Ro_V}$ for all the three boundary types. The "o" marker denotes the δ diagnosed from the ensemble-averaged vortex, and the multitude

of scatter points denote the δ of individual vortex profiles. For both NN and FF types, there is no statistical difference between the updraft and downdraft vortices, due to the symmetry in boundary condition. For both types, the DNS agrees with our prediction that $\delta \propto \mathrm{Ro_V}$, even when $\mathrm{Ro_V}$ is as large as 1. The DNS confirms that the δ of NN type is a bit larger than FF type, as will be explained in section IV. This result is robust for different sampling time, though in general the difference between the FF and NN types is hard to identify at $\mathrm{Ro_V} < 0.5$. This is probably technically due to the uncertainty in vortex detection, or theoretically due to the slightly different shape of the ω_z vertical profile that blurs the $\delta - \mathrm{Ro_V}$ relation. For NF type, DNS not only confirms the quasi-linear $\delta - \mathrm{Ro_V}$ trend, but also the prediction that δ is smaller for updraft and larger for downdraft by roughly a constant. The slope ($\delta^{(1)}$ part) is captured well, but the theory seems to underestimate $|\delta^{(0)}|$. The deviation probably lies in Eq. (20) which requires the symmetry of updraft and downdraft but is not met for NF type. Note that as ω_z is not a perfectly linear profile, different measures of $\Delta\omega_z$ and $\overline{\omega_z}$ can lead to different δ magnitude. For example, if δ is diagnosed as the height where the ensemble-averaged ω_z curve crosses $\omega_z = 0$, the δ magnitude is systematically larger than the current method by around 50%, but the trend does not change.

The model is further validated by comparing the ω_z equation budget of the DNS data and theory, as is shown in Fig. 4. The agreement is good within the fluid interior (outside of the boundary layer) where the theory works, and is even better as Ro goes smaller.

IV. UNDERSTANDING δ FOR THREE TYPES OF BOUNDARY CONDITIONS

In this section, we try to interpret the expression $\delta \approx \delta^{(0)} + \mathrm{Ro_V}\delta^{(1)}$ for the three boundary types: δ_{FF}, δ_{NN} and δ_{NF}.

A. Lower free-slip and upper free-slip (FF)

The asymmetry in FF type solely depends on the interior dynamics. Here δ is proportional to $\mathrm{Ro_V}$, and does not depend on E and Γ:

$$\delta_{\mathrm{FF}} = \frac{1}{12}\mathrm{Ro_V}. \tag{34}$$

The $w^{(0)}$ is proportional to $\alpha\mathrm{E}/\Gamma^2$, so the vertical advection and stretching of ω_z, which are asymmetric factors and are also associated with $w^{(0)}$, are also proportional to $\alpha\mathrm{E}/\Gamma^2$. In the

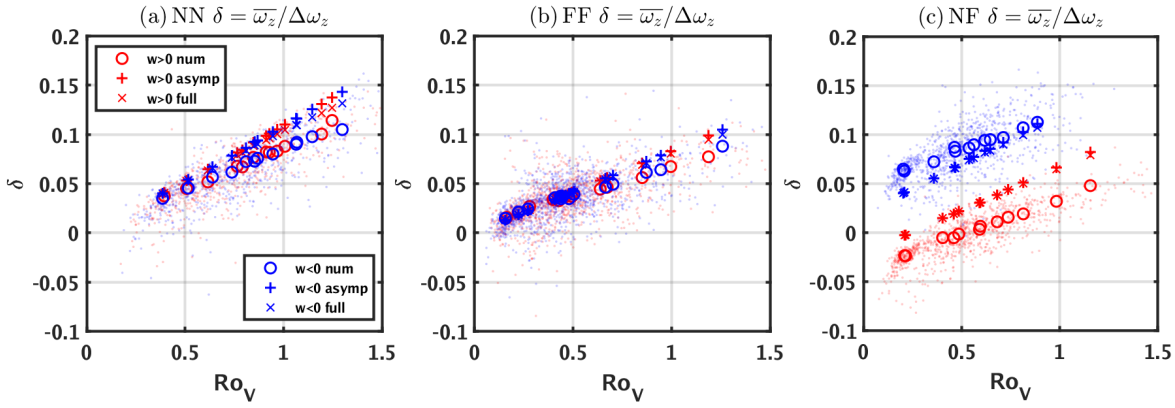

FIG. 8. The relationship between δ and $\mathrm{Ro_V}$ for (a) NN type tests, (b) FF type tests and (c) NF type tests. Data throughout EXP 1-16 are used. The "o" stands for the ensemble average result from DNS, the "+" stands for the asymptotic analytical solution $\delta = \delta^{(0)} + \mathrm{Ro_V}\delta^{(1)}$ that uses the unsimplified Eqs. (28) and (31), and the "x" stands for the numerical solution of the nonlinear eigenvalue problem. The scatter points stand for the δ calculated with individual vortex profiles, which are diagnosed from the DNS. The red markers stand for the updrafts, and the blue markers stand for the downdrafts.

first order equation (30), such asymmetry is balanced by the asymmetric horizontal diffusion which is also proportional to $\alpha \mathrm{E}/\Gamma^2$. Thus, the $\alpha \mathrm{E}/\Gamma^2$ in $\delta^{(1)}$ cancels out. Physically, the asymmetry is due to the larger absolute vorticity stretching in the cyclonic region that favors positive vorticity production, as well as the vertical advection of ω_z that "pushes" the ω_z profile toward the anticyclonic side to produce a shift of δ. That the vortex becomes thinner at the cyclonic side provides a stronger horizontal diffusion to balance the extra positive

vorticity production there, helping reduce the asymmetry.

B. Lower no-slip and upper no-slip (NN)

The δ here clearly shows the dominant role of the fluid interior contribution ($\mathrm{Ro_V}/12 \approx 0.083\mathrm{Ro_V}$) which is already seen in the FF type, and a smaller correction ($0.024\mathrm{Ro_V}$ for EXP 4) due to the Ekman layers which introduces the dependence on E and Γ:

$$\delta_{\mathrm{NN}} = \left[\frac{1}{12} + \underbrace{\frac{\left(\frac{\mathrm{E}}{2}\right)^{1/2}\left(\frac{1}{3}+\frac{\gamma}{2}\right)}{\frac{2\alpha\mathrm{E}}{\Gamma^2} + 2\left(\frac{\mathrm{E}}{2}\right)^{1/2}}}_{\text{correction}} \right] \mathrm{Ro_V} > \delta_{\mathrm{FF}}. \tag{35}$$

For given $\mathrm{Ro_V}$, δ_{NN} is always larger than δ_{FF}. On one hand, the lower and upper Ekman layer systematically raise the updraft strength, which enhance the vertical advection of ω_z. Such an asymmetric tendency is partly balanced by the horizontal diffusion whose strength is proportional to Γ^{-2}, so a thinner vortex with a smaller Γ has a lower δ_{NN}.

On the other hand, the stronger vorticity and therefore the Ekman pumping anomaly at the cyclonic side suppresses the asymmetry (the $2(\mathrm{E}/2)^{1/2}$ part in the denominator of the correction term), because it makes the fluid interior w increment which is responsible for stretching smaller than the w decrement for squeezing. This effect also has its limitation. For a cyclone, the centrifugal effect (γ) reduces the efficiency for pumping mass with given vorticity, so the difference between the w increment near the lower boundary and the decrement near the upper boundary is mitigated.

The correction term can be simplified by substituting in the $\Gamma \sim \mathrm{E}^{1/3}$ law, and dividing both the numerator and denominator by $\mathrm{E}^{1/2}$. Now, only the first term in the denominator has a $\mathrm{E}^{-1/6}$ dependence on E. As "$-1/6$" is quite smooth a slope, the correction term is quite close to a constant.

In summary, the gross effect of the two Ekman layers is enhancing asymmetry. The direct effects of Γ and E in Eq. (35) are much less influential than $\mathrm{Ro_V}$.

C. Lower no-slip and upper free-slip (NF)

One may consider the NF type as an extreme case of a differential Ekman pumping/suction of the lower and upper plates, as is mentioned in analyzing the NN type. Here

the approximate expression of δ under $\delta^{(0)} \ll 1$ is:

$$\delta_{\mathrm{NF}} \approx \delta^{(0)} + \left\{ \frac{1}{12} + \frac{\frac{5}{12}\left(\frac{\mathrm{E}}{2}\right)^{1/2}}{\frac{2\alpha\mathrm{E}}{\Gamma^2} + \left(\frac{\mathrm{E}}{2}\right)^{1/2}} + \frac{\epsilon_w \delta^{(0)} \frac{\alpha \mathrm{E}}{\Gamma^2}}{\frac{2\alpha\mathrm{E}}{\Gamma^2} + \left(\frac{\mathrm{E}}{2}\right)^{1/2}} + \frac{\frac{\gamma}{4}\left(\frac{\mathrm{E}}{2}\right)^{1/2}}{\frac{2\alpha\mathrm{E}}{\Gamma^2} + \left(\frac{\mathrm{E}}{2}\right)^{1/2}} \right\} \mathrm{Ro_V}, \tag{36}$$

where $\delta^{(0)}$ can be simplified using $\mathrm{E} \sim 10^{-4}$ and $\Gamma \sim 0.2$, as well as the $\Gamma \sim \mathrm{E}^{1/3}$ law :

$$\delta^{(0)} = -\frac{\epsilon_w}{4\sqrt{2}\alpha\Gamma^{-2}\mathrm{E}^{1/2} + 2} \approx -\frac{\epsilon_w}{4\sqrt{2}\alpha}\Gamma^2\mathrm{E}^{-1/2} \sim \mathrm{E}^{1/6}. \tag{37}$$

Thus, $\delta^{(0)}$ is a quite fixed quantity, with the EXP 4 case rendering $\delta^{(0)} \approx -0.03\epsilon_w$. The $\delta^{(0)}$ is positive for downdraft and negative for updraft. To explain this, first consider an updraft. The bottom Ekman pumping gives the parcel some $w^{(0)}$, but when it approaches the upper plate, $w^{(0)}$ needs to decrease all the way to 0. As a result, the stretching of background vorticity is weaker than squeezing, which makes its ω_z more negative. Oppositely, there is extra stretching for downdraft, which makes its ω_z more positive.

As for $\delta^{(1)}$ which is in the large bracket of Eq. (36), the first term (1/12) is the role of fluid interior. The second and third term, as a whole, denote the enhancement of vertical advection and therefore asymmetry by the single side Ekman pumping/suction vertical velocity. The fourth term is the nonlinear effect in Ekman pumping which is trivial. For the updraft of EXP 4 run, the values of the four terms of the approximated $\delta^{(1)}$ are: 0.083 (the 1/12), 0.024, -0.014, 0.003. The second to fourth terms are close to constants, as can be seen by substituting $\Gamma \sim \mathrm{E}^{1/3}$ into Eq. (36).

Another possibly more accurate way to calculate $\delta^{(0)}$ is solving the neutral mode of the linear stability problem [16, 26] with NF type boundary condition, but an explicit expression is unlikely to be found. This is left for future work.

V. CONCLUSION

We study the asymmetry of cyclones and anticyclones for rotating convection between two parallel plates, specifically in its "cellular regime" where convection is weak and rotation is strong. The rotation shapes convection into densely packed vertically-aligned vortices, which are of comparable magnitude and in quasi-steady state. The updraft (downdraft) vortices are cyclonic (anticyclonic) at the lower level and anticyclonic (cyclonic) at the upper level. Portegies et al. [26] derived a linear model of convective vortex between two no-slip plates. They showed that the vertical vorticity ω_z at the vortex center is quasi-linear with height.

A clear shift of the vortex center ω_z profile toward the cyclonic side (i.e. the magnitude of positive ω_z is larger than the negative ω_z) was observed but remains unexplained. In this work, a simple model is presented to explain such asymmetry in the cellular regime.

The observation that vortex center ω_z profile is quasi-linear with height is explained with the thermal wind relation and the advection-diffusion of temperature. This constraint enables us to focus on ω_z equation. The complex dynamic-thermodynamic coupling is only used for determining the convective strength which is characterized by the vorticity difference $\Delta\omega_z$ between the cyclonic and anticyclonic ends. The parameter $\Delta\omega_z$ is considered to be known a priori, and is represented as vorticity Rossby number $\mathrm{Ro_V} = \Delta\omega_z/f_e$, which can be either diagnosed from direct numerical simulation (DNS) or potentially from the existing theoretical models of convective amplitude [21, 28]. The parameter $\mathrm{Ro_V}$, together with the vortex aspect ratio Γ and Ekman number E, renders an analytical model of the asymmetry factor $\delta = \overline{\omega_z}/\Delta\omega_z$ ($\overline{\omega_z}$ is the vertically averaged ω_z) based on the balanced dynamics of ω_z alone.

Physically, the asymmetry in the cellular regime is contributed from both the fluid interior and Ekman layer dynamics. As for the fluid interior within a vortex column, the downgradient vertical advection of ω_z "pushes" its profile toward the anticyclonic side to enhance the cyclonic part. Meanwhile, the stretching of absolute vertical vorticity $(\omega_z + f_e)$ is more efficient at the cyclonic side. Such positive ω_z production makes the cyclonic side stronger and compacter. A compacter cyclone has a stronger horizontal diffusion of vorticity, so the feedback on vortex shape offsets some of the asymmetry. As a result, we get $\delta \approx \mathrm{Ro_V}/12$ for a vortex between two free-slip plates (FF type), without the influence of Ekman layer. Such quasi-linear dependence of δ on $\mathrm{Ro_V}$ is valid even when $\mathrm{Ro_V}$ is as large as 1. The boundary layer effect is studied for a vortex between two no-slip plates (NN type). It turns out to be a minor modification to the asymmetry problem compared to the interior dynamics. The Ekman pumping (suction) at the cyclonic (anticyclonic) side elevates the vertical velocity strength, which enhances the interior asymmetry produced by the vertical advection of ω_z. However, the pumping and suction strength difference also matters. Because a cyclone is generally stronger, the stronger pumping (weaker suction) leaves less w increment for vorticity stretching than squeezing in fluid interior, so the original cyclonic tendency is offset a bit. Another difference is due to the relatively weak nonlinear vertical advection and stretching of ω_z in the Ekman layer, which makes cyclones pump less ver-

tical velocity than anticyclones, and therefore slightly favors the asymmetry. An extreme case is the vortex between a no-slip and a free-slip plate (NF type). The stretching and squeezing outside of the Ekman layer are asymmetric even for the small-amplitude problem where $\mathrm{Ro_V} \to 0$. This makes the updraft (downdraft) stretches (squeezes) less and squeezes (stretches) more, and therefore renders a baseline negative (positive) δ that depends on the aspect ratio Γ and E but not $\mathrm{Ro_V}$. We argue that the previous asymmetry explanations [1, 6, 18, 30, 32, 33], which emphasize the role of Ekman pumping in generating vorticity at the cyclonic side and the turbulent mixing in diluting vorticity at the anticyclonic side, is not suitable for the non-turbulent cellular regime.

The DNS result is consistent with our theory of δ, though a little underestimation of the baseline δ magnitude for NF type (named $\delta^{(0)}$) exists. The DNS agrees with the theoretical result that w peaks at the anticyclonic side for NN and FF types, but the theory underestimates the magnitude of this asymmetric feature. One flaw of the theory is the treatment of vorticity horizontal diffusion for NF type.

In future, whether the theory of δ is robust for different Prandtl number Pr needs to be checked, though Pr does not appear in the analytical model. The theory might be extended to consider non-Boussinesq effects such as the variable density (anelastic) effect [44, 45] and the dependence of viscosity on temperature [46]. In a macroscopic view, the modeling framework is only a small step toward understanding cyclone/anticyclone asymmetry, because it only applies to the non-turbulent quasi-steady regime where the asymmetry factor δ and vorticity Rossby number $\mathrm{Ro_V}$ are well-defined. By linking δ to other more general asymmetry norms such as skewness, a connection to the general asymmetry problem in more turbulent regimes would be possible.

ACKNOWLEDGMENTS

The authors thank Zhiming Feng, Mingrui Liu, and Yunjiao Pu for the cooperative work on constructing a rotating convection apparatus, which provided the initiative inspiration for this purely numerical-based work. We thank Prof. Yuan Wang, Prof. Bowen Zhou, Prof. Yonghua Pan, Prof. Huibin Gao, Prof. Xin Xu and Prof. Yihua Lin for the generous support. We thank Prof. Leif Thomas, Prof. Shengqi Zhou, Prof. Wei Wang and Prof. Morgan O'Neill for fruitful discussion. We thank Prof. Ian

Grooms and Dr. Junqiang Shi for helpful advice. We thank the Stanford Research Computing Center for providing computational resources. The CM1 model is available at: https://www2.mmm.ucar.edu/people/bryan/cm1/. All the MATLAB postprocessing code (e.g., theoretical model, vortex center detection) used in this paper, as well as a derivation note can be downloaded from: https://stanford.box.com/s/mju7ipvkllqn0zhxorn8fkout161x5ib.

Appendix A: The adaptation of CM1 to Rayleigh-Bénard problem

The CM1 code is run in its Boussinesq formulation. It uses finite-difference discretization, with 5^{th} order WENO scheme for temperature and velocity advection (only on the final Runge-Kutta step for velocity). All simulations use a $200 \times 200 \times 100$ mesh and a time step of 0.0005. The mesh is horizontally uniform, and vertically nonuniform with refinement near the two boundaries. Fig. 8 shows that the average distance between a cold and warm vortex is at least $0.15H_e$ which corresponds to 12 grid points, so the horizontal resolution is enough. The vertical mesh generation function is: $z_k = (1/2)\tanh(\hat{z}_k)/\tanh(z_0)$, where $z_0 = 2.2$, $\hat{z}_k = -z_0 + (k-1)\, 2z_0/N_z,\ k = 0,\ 1,\ \ldots,\ N_z$. Here $N_z = 100$ is the vertical cell number. For $\mathrm{E} = 10^{-4}$ which means Ekman layer depth $h_E = H_e(2\mathrm{E})^{1/2} \approx 0.014H_e$, there are nine grid points within each Ekman layer.

The CM1 code is modified from its configured "Rayleigh-Bénard convection case". Specifically, the following subroutines are modified: the vertical mesh is set in "param.F", the buoyancy expression is set in "solve.F" and the basic state profile is set in "base.F". The code has been benchmarked with critical Rayleigh number test for the FF type, using EXP 14 - EXP 16.

Appendix B: The method of vortex center detection

As the vortex is not strictly vertically aligned, the vortex center line is approximated as a straight line that crosses a detected vortex center at the lower and upper level.

We choose $z/H_e = \pm 0.484$ as the two horizontal slices for vortex detection. They are deep inside the lower and upper Ekman layer, where both cyclones and anticyclones are easy to distinguish. There are 4 steps.

Firstly, for each slice we use the Q criterion to circle out some "vortical area" and find

all the vorticity extremum within it. The vortical region is defined as the place where the horizontal velocity gradient tensor $\nabla_h \mathbf{u_h} = \partial_i u_j,\ i,j \in \{1,2\}$ has complex eigenvalues [1, 27]. This is equivalent to finding the $Q_{2D} > 0$ place where:

$$Q_{2D} = 4\mathrm{det}\left(\nabla_h \mathbf{u_h}\right) \ - \left[\mathrm{Tr}\left(\nabla_h \mathbf{u_h}\right)\right]^2. \tag{B1}$$

Here "det" means the determinant, "Tr" means the trace.

Secondly, within $Q_{2D} > 0$ region, we pick out all the maximum ω_z position as candidate CC centers and minimum ω_z position as AC centers. If the distance of two vortices is smaller than 0.0375, it is judged as an overlap event and one of the vortex is discarded.

Thirdly, the candidate vortex centers at the two horizontal slices are paired: a CC (AC) at the lower slice and an AC (CC) at the upper slice constitute an updraft (downdraft). The criterion for pairing is that the two vortices' distance projected onto the horizontal plane is smaller than $0.06H_e$ which is a substantial portion of the vortex width. The detected vortex centers that fail to meet the paring criterion are not used for generating profiles.

Fourthly, for each vortex pair, the vortex center line is chosen as the straight line that crosses their centers. Then the w, ω_z and $\nabla_h^2 \omega_z$ are sampled on these lines.

A byproduct of vortex detection is the vortex number density, which is used by Sakai [21] to calculate the characteristic distance between an updraft and downdraft L_d. On each horizontal slice, L_d is related to the total vortex number N from the second step (updraft plus downdraft, and no need to be paired) via:

$$L_d = L_0 / N^{1/2}. \tag{B2}$$

Here $L_0 = 2.5$ is the domain width. In data processing, L_d is further calculated as the average between the $L_0/N^{1/2}$ at the lower and upper slices.

The ensemble-averaged vortex profile of Portegies et al. [26] at $\mathrm{Ra} = 2.5 \times 10^6$, $\mathrm{E} = 10^{-4}$ and $\mathrm{Pr} = 1$ shown in their Fig. 6 is compared with the detection result of EXP 4 in Fig. 3(a) and (g). The agreement is good, so both the detection method and the DNS solver with no-slip boundary condition are validated.

Appendix C: The Ekman layer parameterization

Here we introduce the derivation of Eq. (13). Hart [43] used regular perturbation expansion to derive the bottom Ekman layer pumping relation for a circular vortex. Truncated to

the first order, it is:

$$w_b \approx \frac{h_E}{2}\left\{\frac{\partial V}{\partial r}+\frac{V}{r}-\frac{1}{20 f_e r}\left[9V\frac{\partial V}{\partial r}+7rV\frac{\partial^2 V}{\partial r^2}+7r\left(\frac{\partial V}{\partial r}\right)^2\right]\right\}. \tag{C1}$$

Here $h_E = (2\nu_e/f_e)^{1/2} = (2\mathrm{E})^{1/2}H_e$ is the characteristic depth of Ekman layer, V is the fluid interior tangential velocity, w_b is the pumping vertical velocity at an infinite height and r is the distance to the vortex center. We are only interested in the relation at the vortex center. The V and its derivatives are replaced by vorticity via assuming the vorticity radial profile to be zeroth order Bessel function $J_0(kr)$ which is suitable for the columnar vortices in the cellular regime of RRBC [26]. As the flow close to the vortex center can be approximated as rigid body rotation, we have:

$$\frac{\partial V}{\partial r} \approx \frac{V}{r} \approx \frac{\omega_z}{2} \quad \text{at } r \to 0. \tag{C2}$$

As $\partial\omega_z/\partial r \sim dJ_0(kr)/dr|_{r=0} = -kJ_1(0) = 0$, there is:

$$\frac{\partial^2 V}{\partial r^2}|_{r=0} = \frac{\partial \omega_z}{\partial r}|_{r=0} - \frac{1}{r}\left(\frac{\partial V}{\partial r}|_{r=0} - \frac{V}{r}|_{r=0}\right) = 0. \tag{C3}$$

Substituting Eqs. (C2) and (C3) into Eq. (C1), we get:

$$w_b = \frac{h_E \omega_z}{2}\left(1-\gamma\frac{\omega_z}{f_e}\right). \tag{C4}$$

Here $\gamma = 1/5$ is a constant that signifies the nonlinear effect. The derivation for the upper plate Ekman layer is similar, with a flip of sign at the right-hand-side of Eq. (C4).

The formula for the bottom Ekman layer is validated with Ro = 0.158 (EXP 4) and Ro = 0.132 (EXP 8), NN boundary type simulations, using vortex center ω_z and w profile (Fig. 9). These vortices are detected at $z/H_e = -0.484$ which is near the top of the bottom Ekman layer, a height where the vortical structure of both updraft and downdraft vortices are clear. As we are only interested in the Ekman layer, any profile is sampled on a vertical plumb line, unlike the tilted sampling line for studying the full profiles introduced in Appendix B.

Here we validate Eq. (C4) with the DNS result. Fig. 9 shows that w and ω_z keep changing with height above the Ekman layer (especially for downdraft vortices), so a strict comparison with formula is hard. We choose the w and ω_z data at the height of maximum $|\omega_z|$ (within $3.4h_E$, or 19 grid points from the bottom) for comparison, as is shown in Fig. 10. This height is chosen because the $\Delta\omega_z$ is calculated as the difference of ω_z maximum and minimum.

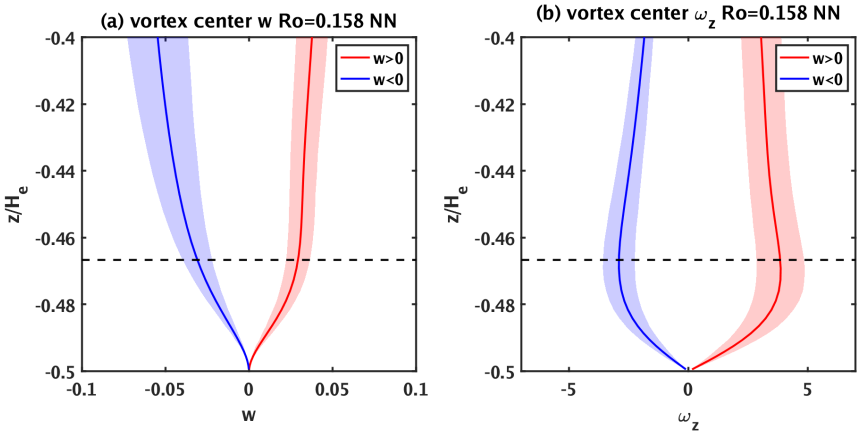

FIG. 9. The vortex center vertical profile of (a) w and (b) ω_z for NN boundary type simulation of Ro = 0.158 (EXP 4). The solid red (blue) lines denote the ensemble-averaged updraft (downdraft) values, and the red shadow denotes the ± 1 standard deviation band. The dashed black line is $z/H_e = -1/2 + (3\pi/4)h_E/H_e$ which is the maximum $|\omega_z|$ predicted by the linear Ekman layer theory [9]. It is a bit above the maximum $|\omega_z|$ observed in the plots.

The asymmetry of the pumping relation of CC and AC is clear and the extent of asymmetry is captured by (C4), despite the deviation in the magnitude of predicted w_b which can be eliminated by tuning (lowering a little bit) the sampling height. The symmetry breaking is more prominent for the more nonlinear Ro = 0.158 (EXP 4) case than the Ro = 0.132 (EXP 8) case.

Appendix D: Why the vortex center ω_z profile is quasi-linear with height?

Here we physically explain how the temperature structure leads to the robust quasi-linear ω_z structure for both small and large magnitude temperature anomaly. The idea is illustrated in Fig. 5 as a schematic diagram. Let $\overline{\theta}(z)$ be the diffusive-equilibrium basic state profile. The thermal wind vorticity equation which links $\partial\omega_z/\partial z$ and $\nabla_h^2\theta'$ is valid under geostrophic balance which is the first order balance in fluid interior in the cellular regime,

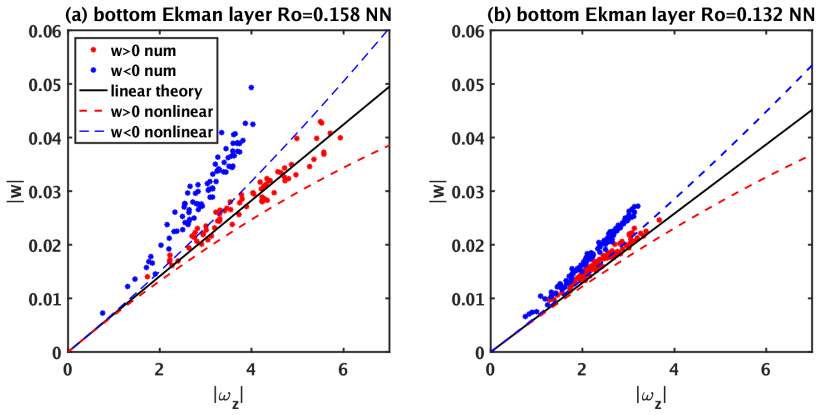

FIG. 10. The scatter plots of the vortex center $|w|$ and $|\omega_z|$ value at the maximum $|\omega_z|$ height (within $3.4h_E$, or 19 grid points from the bottom) of each sampled vortex, with (a) NN boundary type simulation of Ro = 0.158 (EXP 4) and (b) Ro = 0.132 (EXP 8). The reason for using absolute value is to facilitate the comparison between updraft (CC) and downdraft (AC). The red "*" denotes the sampled value from updraft vortices of DNS, and the blue "*" denotes that for downdraft. The dashed red line denotes the nonlinear Ekman pumping velocity Eq. (C4) for an updraft (CC), and the dashed blue line denotes that for a downdraft (AC). The solid black line is the relationship between w and ω_z predicted by the linear Ekman pumping formula $w_b = h_E\omega_z/2$.

and hydrostatic balance which is not fully satisfied at updraft centers in the fluid interior [39]:

$$f_e\frac{\partial \mathbf{u}}{\partial z} \sim \widehat{\mathbf{z}}\times\nabla\theta' \quad \Rightarrow \quad \nabla_h^2\theta' \sim f_e\frac{\partial\omega_z}{\partial z}. \tag{D1}$$

Note that if the centrifugal acceleration is taken into account (gradient wind balance), the right part of Eq. (D1) is only valid right at the vortex center where tangential velocity is zero. As warm core updrafts and cold core downdrafts surround each other, the $\nabla_h^2\theta'$ depends on the θ' difference between a pair of neighboring updraft and downdraft, as well as the characteristic vortex distance L_d:

$$\nabla_h^2\theta' \sim -\frac{\theta'^{\uparrow}(z)-\theta'^{\downarrow}(z)}{L_d^2} \text{ for updraft}, \quad \nabla_h^2\theta' \sim -\frac{\theta'^{\downarrow}(z)-\theta'^{\uparrow}(z)}{L_d^2} \text{ for downdraft}, \tag{D2}$$

where $\theta'^{\uparrow}(z)$ denotes the perturbed updraft center temperature profile and $\theta'^{\downarrow}(z)$ denotes that of a downdraft. Meanwhile, as the updraft and downdraft are governed by the same dynamics for a symmetric boundary condition such as FF and NN (and a bit less for NF), it yields:

$$\theta'^{\uparrow}(z) = -\theta'^{\downarrow}(-z). \tag{D3}$$

Substitute Eqs. (D2) and (D3) into Eq. (D1):

$$\frac{\partial \omega_z}{\partial z} \sim \frac{1}{f_e}\nabla_h^2\theta' \sim \begin{cases} -\frac{1}{f_e}\frac{\theta'^{\uparrow}(z)-\theta'^{\downarrow}(z)}{L_d^2} = -\frac{1}{f_e}\frac{\theta'^{\uparrow}(z)+\theta'^{\uparrow}(-z)}{L_d^2} & \text{updraft} \\ -\frac{1}{f_e}\frac{\theta'^{\downarrow}(z)-\theta'^{\uparrow}(z)}{L_d^2} = -\frac{1}{f_e}\frac{\theta'^{\downarrow}(z)+\theta'^{\downarrow}(-z)}{L_d^2} & \text{downdraft.} \end{cases} \tag{D4}$$

Thus, $\partial\omega_z/\partial z$ should be close to an even function of z. In an updraft, $\theta'^{\uparrow}(z)$ is positive at all levels due to the upward transport of warm fluid, so $\partial\omega_z/\partial z$ is negative at all z, and vice versa for a downdraft.

Next, we explore θ' structure at small and large w limits more closely. The vortex center temperature equation is a steady advection-diffusion equation:

$$w\frac{\partial\theta'}{\partial z} + w\frac{d\overline{\theta}}{dz} = \kappa_e\nabla_h^2\theta' + \kappa_e\frac{\partial^2\theta'}{\partial z^2} \approx \kappa_e\nabla_h^2\theta'. \tag{D5}$$

Here the vertical diffusion has been neglected due to the small aspect ratio of the vortex. The relative role of advection and horizontal diffusion can be quantified with Peclect number, which is the ratio of horizontal diffusion time scale L_d^2/κ_e to convective time scale H_e/W_e:

$$\mathrm{Pe} \equiv \frac{L_d^2}{H_e^2}\frac{W_e H_e}{\kappa_e}. \tag{D6}$$

Here W_e is the effective vertical velocity scale, which can be estimated with the balance of background vorticity stretching and the horizontal diffusion of vorticity in the fluid interior:

$$f_e\frac{\partial w}{\partial z} \sim -\nu_e\nabla_h^2\omega_z \quad \Rightarrow \quad f_e\frac{W_e}{H_e} \sim \nu_e\alpha\frac{\Delta\omega_z}{L_d^2}. \tag{D7}$$

Here $\alpha = 23$ is the same as that used in Eq. (21), and $\Delta\omega_z$ is the vorticity difference between the CC/AC ends. Substituting Eq. (D7) into Eq. (D6), we get:

$$\mathrm{Pe} \sim \alpha \mathrm{Ro_V Pr}. \tag{D8}$$

For cellular regime, $\mathrm{Ro_V} \lesssim O(1)$, so $\mathrm{Pe} \lesssim O(10^1)$ for our $\mathrm{Pr} = 1$ case, thus advection is dominant unless $\mathrm{Ro_V} < 0.1$ where convection is very weak.

The small Pe limit which corresponds to $\mathrm{Ro_V} \ll 1$ and small $\widetilde{\mathrm{Ra}}$ is a small-amplitude regime, where the normal mode solution of Portegies et al. [26] works. The main balance is between the vertical advection of basic state temperature and horizontal diffusion:

$$w\frac{d\bar{\theta}}{dz} \sim \kappa_e \nabla_h^2 \theta' \sim -\frac{\kappa_e}{L_d^2}\theta'. \tag{D9}$$

Thus, the vertical profile of θ' should be proportional to w whose largest magnitude is at the middle layer. Suppose $w \sim \cos(\pi z)$ in this linear regime, Eq. (D7) shows that the vertical variation of ω_z at small w limit is controlled by $\sin(\pi z)$. If there are Ekman layers, w will be more uniform in the fluid interior because Ekman pumping and suction have systematically elevated the magnitude of w. The more vertically uniform w is, the more vertically linear θ' and therefore ω_z should be.

For large Pe, which corresponds to large $\widetilde{\mathrm{Ra}}$, the nonlinear vertical advection dominates diffusion. The temperature contour surface is pushed toward the upper (lower) plate by updraft (downdraft), producing a strong temperature vertical gradient near the arrival boundary and a weak one in the fluid interior. Thus, temperature is vertically uniform within the vortex, and the temperature difference between updraft and downdraft cores are invariant with height. Eq. (D5) shows that θ' is now linear with z:

$$w\frac{\partial\theta'}{\partial z} + w\frac{d\bar{\theta}}{dz} \sim 0 \quad \Rightarrow \quad \frac{\partial\theta'}{\partial z} \sim -\frac{d\bar{\theta}}{dz} = 1. \tag{D10}$$

According to Eq. (D4), $\partial\omega_z/\partial z$ is now constant in the fluid interior. Thus, we expect that ω_z is approximately linear with z in both small and large Pe (or $\widetilde{\mathrm{Ra}}$) regime, so long as the vortices are still columnar and densely packed.

Appendix E: The numerical technique to solve the full nonlinear problem

The solution to Eq. (24) that only satisfies the lower boundary condition is:

$$w^+(z) = \left[z - \epsilon_w\left(\delta + \mathrm{Ro_V^{-1}}\right)\right]\left[\mathrm{C} + \frac{\alpha \mathrm{E}}{\Gamma^2 \mathrm{Ro_V}}\left\{\ln\left[z - \epsilon_w\left(\delta + \mathrm{Ro_V^{-1}}\right)\right] + \frac{\epsilon_w\left(\delta - \mathrm{Ro_V^{-1}}\right)}{z - \epsilon_w\left(\delta + \mathrm{Ro_V^{-1}}\right)}\right\}\right], \tag{E1}$$

where the integral constant C is:

$$\mathrm{C} = \frac{w^+|_{z=-1/2}}{-1/2 - \epsilon_w\left(\delta + \mathrm{Ro_V^{-1}}\right)} - \frac{\alpha \mathrm{E}}{\Gamma^2 \mathrm{Ro_V}}\left\{\ln\left[-\frac{1}{2} - \epsilon_w\left(\delta + \mathrm{Ro_V^{-1}}\right)\right] + \frac{\epsilon_w\left(\delta - \mathrm{Ro_V^{-1}}\right)}{-1/2 - \epsilon_w\left(\delta + \mathrm{Ro_V^{-1}}\right)}\right\} \tag{E2}$$

Here $w^+|_{z=-1/2}$ is shown in Eq. (24). The solvability condition is enforcing the w^+ predicted by Eq. (E1) at $z = 1/2$ end to satisfy the upper boundary condition. This yields a nonlinear problem to solve δ. The numerical solution is found by traversing δ within $[-0.3, 0.3]$.

---

[1] P. Vorobieff and R. E. Ecke, Turbulent rotating convection: an experimental study, Journal of Fluid Mechanics **458**, 191 (2002).

[2] B. Sreenivasan and P. Davidson, On the formation of cyclones and anticyclones in a rotating fluid, Physics of Fluids **20**, 085104 (2008).

[3] G. J. Hakim, C. Snyder, and D. J. Muraki, A new surface model for cyclone–anticyclone asymmetry, Journal of the atmospheric sciences **59**, 2405 (2002).

[4] L. M. Polvani, J. C. McWilliams, M. A. Spall, and R. Ford, The coherent structures of shallow-water turbulence: Deformation-radius effects, cyclone/anticyclone asymmetry and gravity-wave generation, Chaos: An Interdisciplinary Journal of Nonlinear Science **4**, 177 (1994).

[5] A. Naso, Cyclone-anticyclone asymmetry and alignment statistics in homogeneous rotating turbulence, Physics of Fluids **27**, 035108 (2015).

[6] S.-S. Ding, K. L. Chong, J.-Q. Shi, G.-Y. Ding, H.-Y. Lu, K.-Q. Xia, and J.-Q. Zhong, Asymmetric vorticity distribution induces anomalous vortex motion in rapidly rotating thermal convection, arXiv preprint arXiv:1906.01325 (2019).

[7] J.-Q. Shi, H.-Y. Lu, S.-S. Ding, and J.-Q. Zhong, Fine vortex structure and flow transition to the geostrophic regime in rotating Rayleigh-Bénard convection, Physical Review Fluids **5**, 011501 (2020).

[8] J. Y.-K. Cho and L. M. Polvani, The emergence of jets and vortices in freely evolving, shallow-water turbulence on a sphere, Physics of Fluids **8**, 1531 (1996).

[9] G. K. Vallis, *Atmospheric and oceanic fluid dynamics* (Cambridge University Press, 2017).

[10] I. Yavneh, A. F. Shchepetkin, J. C. McWilliams, and L. P. Graves, Multigrid solution of rotating, stably stratified flows, Journal of Computational Physics **136**, 245 (1997).

[11] G. Perret, A. Stegner, M. Farge, and T. Pichon, Cyclone-anticyclone asymmetry of large-scale wakes in the laboratory, Physics of Fluids **18**, 036603 (2006).

[12] J. Marshall and F. Schott, Open-ocean convection: Observations, theory, and models, Reviews of Geophysics **37**, 1 (1999).

[13] E. A. Hendricks, M. T. Montgomery, and C. A. Davis, The role of "vortical" hot towers in the formation of tropical cyclone diana (1984), Journal of the atmospheric sciences **61**, 1209 (2004).

[14] J. Aurnou, M. Calkins, J. Cheng, K. Julien, E. King, D. Nieves, K. M. Soderlund, and S. Stellmach, Rotating convective turbulence in earth and planetary cores, Physics of the Earth and Planetary Interiors **246**, 52 (2015).

[15] F. Busse and C. Carrigan, Laboratory simulation of thermal convection in rotating planets and stars, Science **191**, 81 (1976).

[16] S. Chandrasekhar, *Hydrodynamic and hydromagnetic stability* (Courier Corporation, 2013).

[17] S. Stellmach, M. Lischper, K. Julien, G. Vasil, J. Cheng, A. Ribeiro, E. King, and J. Aurnou, Approaching the asymptotic regime of rapidly rotating convection: boundary layers versus interior dynamics, Physical review letters **113**, 254501 (2014).

[18] K. Julien, S. Legg, J. McWilliams, and J. Werne, Rapidly rotating turbulent Rayleigh-Bénard convection, Journal of Fluid Mechanics **322**, 243 (1996).

[19] Y. Nakagawa and P. Frenzen, A theoretical and experimental study of cellular convection in rotating fluids, Tellus **7**, 2 (1955).

[20] B. Boubnov and G. Golitsyn, Experimental study of convective structures in rotating fluids, Journal of Fluid Mechanics **167**, 503 (1986).

[21] S. Sakai, The horizontal scale of rotating convection in the geostrophic regime, Journal of Fluid Mechanics **333**, 85 (1997).

[22] H. Rajaei, R. P. Kunnen, and H. J. Clercx, Exploring the geostrophic regime of rapidly rotating convection with experiments, Physics of Fluids **29**, 045105 (2017).

[23] D. Noto, Y. Tasaka, T. Yanagisawa, and Y. Murai, Horizontal diffusive motion of columnar vortices in rotating Rayleigh–Bénard convection, Journal of Fluid Mechanics **871**, 401 (2019).

[24] K. Julien, S. Legg, J. McWilliams, and J. Werne, Plumes in rotating convection. part 1. ensemble statistics and dynamical balances, Journal of Fluid Mechanics **391**, 151 (1999).

[25] M. Sprague, K. Julien, E. Knobloch, and J. Werne, Numerical simulation of an asymptotically reduced system for rotationally constrained convection, Journal of Fluid Mechanics **551**, 141 (2006).

[26] J. Portegies, R. Kunnen, G. van Heijst, and J. Molenaar, A model for vortical plumes in rotating convection, Physics of Fluids **20**, 066602 (2008).

[27] R. Kunnen, H. Clercx, and B. Geurts, Vortex statistics in turbulent rotating convection, Physical Review E **82**, 036306 (2010).

[28] I. Grooms, K. Julien, J. B. Weiss, and E. Knobloch, Model of convective Taylor columns in rotating Rayleigh-Bénard convection, Physical review letters **104**, 224501 (2010).

[29] R. Kunnen, B. J. Geurts, and H. Clercx, Turbulence statistics and energy budget in rotating Rayleigh–Bénard convection, European Journal of Mechanics-B/Fluids **28**, 578 (2009).

[30] R. Kunnen, B. J. Geurts, and H. Clercx, Experimental and numerical investigation of turbulent convection in a rotating cylinder, Journal of fluid mechanics **642**, 445 (2010).

[31] K. Julien, A. Rubio, I. Grooms, and E. Knobloch, Statistical and physical balances in low Rossby number Rayleigh–Bénard convection, Geophysical & Astrophysical Fluid Dynamics **106**, 392 (2012).

[32] B. Favier, L. Silvers, and M. Proctor, Inverse cascade and symmetry breaking in rapidly rotating Boussinesq convection, Physics of Fluids **26**, 096605 (2014).

[33] C. Guervilly, D. W. Hughes, and C. A. Jones, Large-scale vortices in rapidly rotating Rayleigh–Bénard convection, Journal of Fluid Mechanics **758**, 407 (2014).

[34] K. A. Emanuel, *Atmospheric convection* (Oxford University Press on Demand, 1994).

[35] M. Fang and K. K. Tung, A simple model of nonlinear Hadley circulation with an ITCZ: Analytic and numerical solutions, Journal of the atmospheric sciences **53**, 1241 (1996).

[36] M. Fantini, An atmospheric Bénard problem, Quarterly Journal of the Royal Meteorological Society **145**, 469 (2019).

[37] C.-H. Moeng and R. Rotunno, Vertical-velocity skewness in the buoyancy-driven boundary layer, Journal of the Atmospheric Sciences **47**, 1149 (1990).

[38] G. H. Bryan and J. M. Fritsch, A benchmark simulation for moist nonhydrostatic numerical models, Monthly Weather Review **130**, 2917 (2002).

[39] K. Julien, J. M. Aurnou, M. A. Calkins, E. Knobloch, P. Marti, S. Stellmach, and G. M. Vasil, A nonlinear model for rotationally constrained convection with Ekman pumping, Journal of Fluid Mechanics **798**, 50 (2016).

[40] M. Plumley, K. Julien, P. Marti, and S. Stellmach, The effects of Ekman pumping on quasi-geostrophic Rayleigh–Bénard convection, Journal of Fluid Mechanics **803**, 51 (2016).

[41] S.-I. Ishida and T. Iwayama, A comprehensive analysis of nonlinear corrections to the classical Ekman pumping, Journal of the Meteorological Society of Japan. Ser. II **84**, 839 (2006).

[42] R. Wu and W. Blumen, An analysis of Ekman boundary layer dynamics incorporating the geostrophic momentum approximation, Journal of the Atmospheric Sciences **39**, 1774 (1982).

[43] J. E. Hart, A note on nonlinear corrections to the Ekman layer pumping velocity, Physics of Fluids **12**, 131 (2000).

[44] T. M. Rogers, G. A. Glatzmaier, and S. Woosley, Simulations of two-dimensional turbulent convection in a density-stratified fluid, Physical Review E **67**, 026315 (2003).

[45] M. A. Calkins, K. Julien, and P. Marti, The breakdown of the anelastic approximation in rotating compressible convection: implications for astrophysical systems, Proceedings of the Royal Society A: Mathematical, Physical and Engineering Sciences **471**, 20140689 (2015).

[46] J. Zhang, S. Childress, and A. Libchaber, Non-Boussinesq effect: Asymmetric velocity profiles in thermal convection, Physics of Fluids **10**, 1534 (1998).